Science

AAAS

Supplementary Materials for

Information scrambling in quantum circuits

Xiao Mi *et al*.

Corresponding authors: Kostyantyn Kechedzhi, kostyantyn@google.com; Vadim Smelyanskiy, smelyan@google.com; Yu Chen, bryanchen@google.com

The PDF file includes:

Materials and Methods
Supplementary Text
Figs. S1 to S29
References

Materials and Methods

The quantum processor used in this work is the "Sycamore" processor consisting of 53 superconducting transmon qubits coupled with tunable couplers. The fabrication and specification of the quantum processor are described in detail in [38]. The additional gate calibration and error-mitigation techniques for this experiment are described in detail in Section II of the Supplementary Text below.
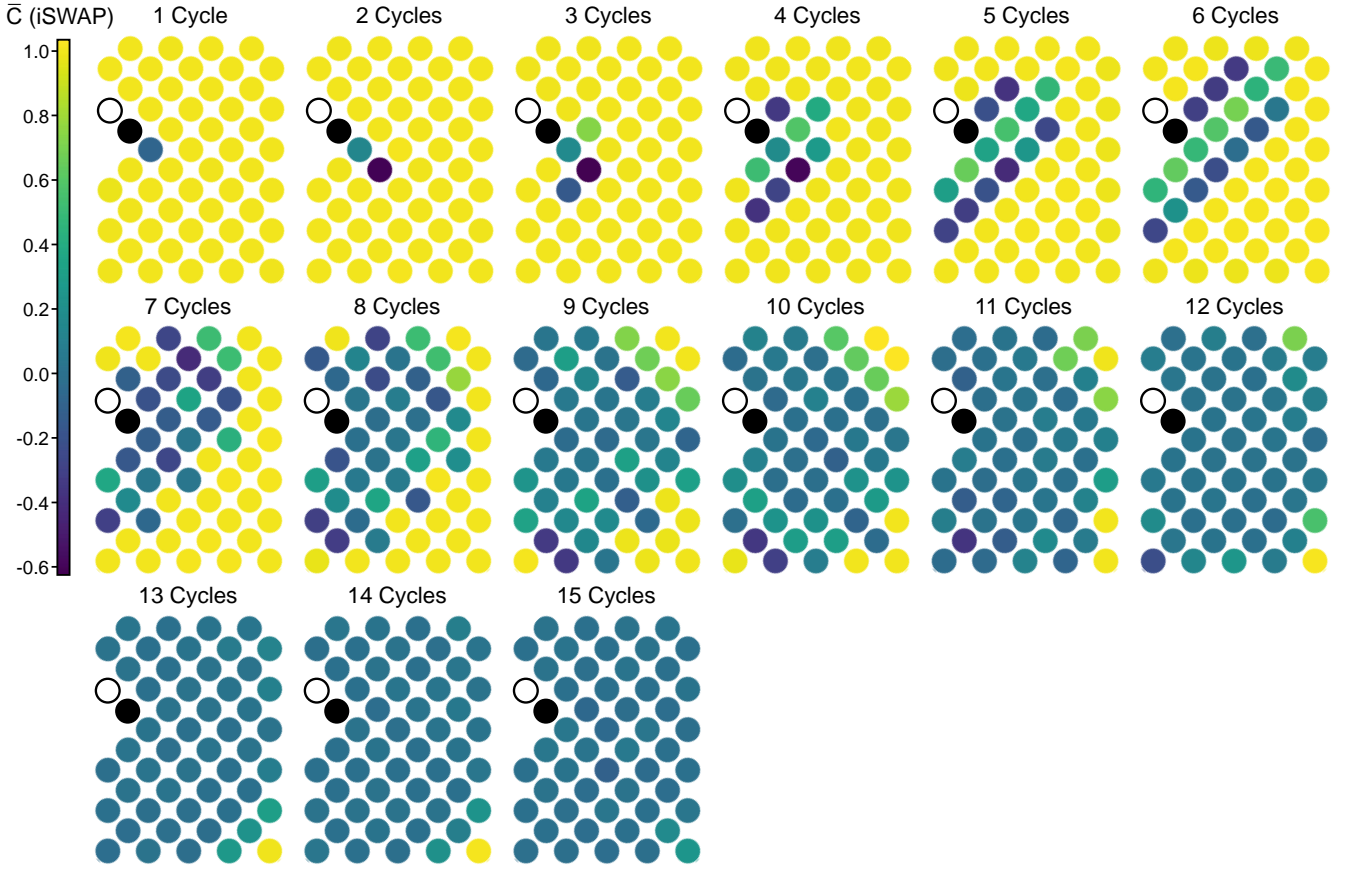
Supplementary Text

CONTENTS

FIG. S1. Full evolution of average OTOCs for iSWAP random circuits. The average OTOCs of the 53-qubit system shown for every cycle up to a total of 15. The black unfilled (filled) circle represents the location of the ancilla (measurement) qubit. The colors of the other filled circles represent the values of $\overline{C}$ for different locations of the butterfly qubit. The two-qubit gate used here is iSWAP and the data are averaged over 38 random circuit instances.

I. EXTENDED DATA

In this section, we provide data not covered in the main text. These include the spatial distribution of average OTOCs on the 53-qubit system, average OTOC behaviors for integrable quantum circuits, measurements of OTOCs in non-random circuits and more detailed investigation of errors in experimental OTOC measurements.

A. Full 53-Qubit Average OTOC Data

Figure S1 shows experimentally measured average OTOCs, $\overline{C}$, for 51 different possible butterfly qubit locations. The data are also shown for every circuit cycle from 1 through 15. Here iSWAP is used as the two-qubit gate. The sharp nature of the wavefront propagation is readily visible, where a large reduction from $\overline{C} = 1$ is observed as soon as the lightcone of the measurement qubit (black filled circle) reaches a given qubit. In comparison, similar data are shown up to a total of 24 circuit cycles for random circuits containing $\sqrt{\text{iSWAP}}$ gates (Fig. S2). The dynamics is seen to be slower than iSWAP, as mentioned in the main text. In particular, the wavefront is also broader, as seen by the more gradual spatial transition from $\overline{C} = 1$ to $\overline{C} \approx 0$.

B. OTOCs for Non-Integrable and Integrable Quantum Circuits

In the main text of this work, we have primarily focused on quantum circuits that are non-integrable [44], i.e. capable of evolving a quantum system into states with maximal degrees of scrambling. In general, many quantum
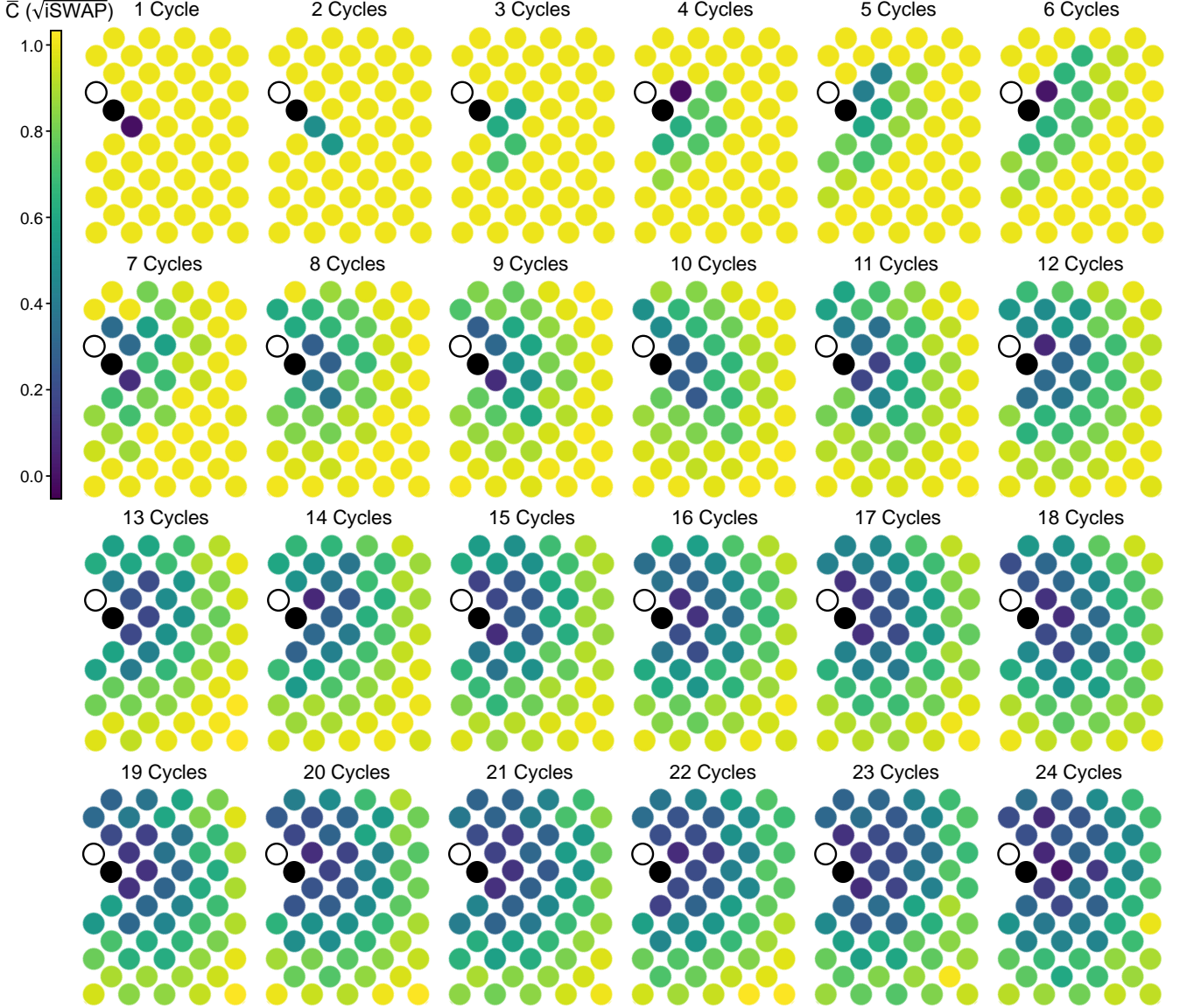
FIG. S2. Full evolution of average OTOCs for $\sqrt{\text{iSWAP}}$ random circuits. The average OTOCs of the 53-qubit system shown for every cycle up to a total of 24. The black unfilled (filled) circle represents the location of the ancilla (measurement) qubit. The colors of the other filled circles represent the values of $\overline{C}$ for different locations of the butterfly qubit. The two-qubit gate used here is $\sqrt{\text{iSWAP}}$ and the data are averaged over 24 random circuit instances.

circuits or dynamical processes are integrable and lead to small degree of quantum scrambling even at long time scales. Examples include Clifford circuits [45], dynamics of free fermions [46] and many-body localization [11]. For certain integrable, pseudo-random circuits such as Clifford circuits, OTOC fluctuation is needed to distinguish them from non-integrable circuits, as demonstrated in the main text. In many other cases, average OTOCs behave differently for integrable quantum circuits compared to non-integrable ones and are sufficient to differentiate between them, which we illustrate next.

Figure. S3 shows two different types of quantum circuits. The circuit in the left panel consists of $\sqrt{\text{iSWAP}}$ gates and single-qubit gates randomly chosen from $\sqrt{X^{\pm}}, \sqrt{Y^{\pm}}, \sqrt{W^{\pm}}, \sqrt{V^{\pm}}$. This is the example of a non-integrable circuit, which is expected to lead to maximal scrambling at long times. The circuit in the right panel has the same two-qubit gates, but the single-qubit gates are replaced with Z gates that have angles randomly chosen from the interval $[-\pi, \pi]$. This is the example of an integrable circuit, where the dynamics does not lead to maximal scrambling if implemented in 1D.

The experimentally measured average OTOCs are shown in Fig. S3B for both types of quantum circuits. Here,
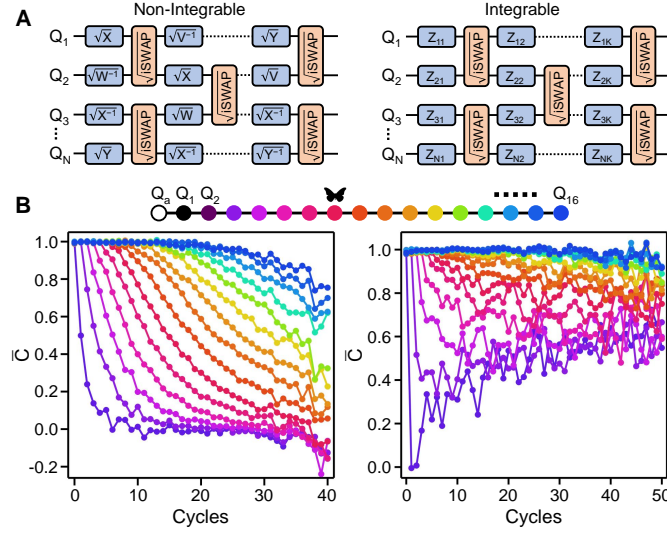
FIG. S3. Average OTOCs for non-integrable and integrable quantum circuits. (A) Two different types of quantum circuits. Left panel shows a non-integrable quantum circuit composed of $\sqrt{\text{iSWAP}}$ and single-qubit gates randomly drawn from $\sqrt{X^{\pm}}$, $\sqrt{Y^{\pm}}$, $\sqrt{W^{\pm}}$, $\sqrt{V^{\pm}}$. Right panel shows an integrable quantum circuit composed of $\sqrt{\text{iSWAP}}$ and single-qubit gates that are rotations around the z-axis of the Bloch sphere with random angles. (B) Average OTOCs $\overline{C}$ for the two types of random circuits, implemented on a 1D chain of 16 qubits. The qubit configuration is shown on top, where the unfilled (filled) black circle represents the ancilla (measurement) qubit Q_a (Q_1). Left panel shows $\overline{C}$ with the butterfly qubit corresponding to qubits Q_2 through Q_{16}, where the random circuits are of the type described in the left panel of (A). Right panel shows similar data for the random circuits of the type in the right panel of (A). The locations of the butterfly qubit are indicated by the colors of the data symbols and the legend on top. All data are averaged over 40 circuit instances.
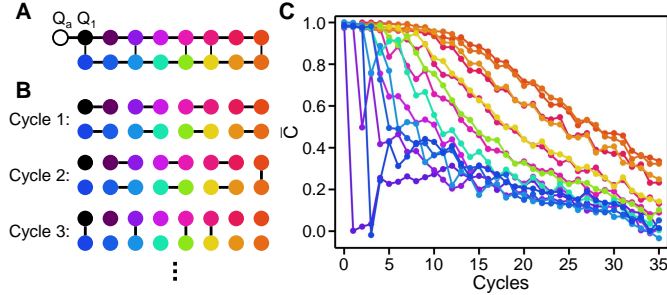

FIG. S4. Transition into non-integrability in the XY Model. (A) A 2D arrangement of qubits in the form of two parallel 1D chains with 5 connections between each other. Black unfilled (filled) circle denotes the ancilla (measurement) qubit Q_a (Q_1). (B) Order for applying the two-qubit gates $\sqrt{\text{iSWAP}}$. The qubit connections denote the $\sqrt{\text{iSWAP}}$ gates that are applied for a particular cycle. Additional cycles repeat the first three cycles, e.g. cycle 4 applies the same $\sqrt{\text{iSWAP}}$ gates as cycle 1 and so on. (C) Average OTOCs $\overline{C}$ with the butterfly qubit corresponding to qubits Q_2 through Q_{16}. The locations of the butterfly qubit are indicated by the colors of the data symbols and the colors of the qubits in (A) and (B). All data are averaged over 36 circuit instances.

the two-qubit gates are applied in a brick-work pattern similar to what is used in Fig. 1C of the main text. For the non-integrable circuits, we observe a clear propagation of the OTOCs along with a diffusive broadening of the wavefronts, similar to what was observed in Fig. 2C of the main text. In particular, $\overline{C}$ monotonically decays toward 0 at large circuit cycles. On the other hand, $\overline{C}$ does not show the wave-like propagation for the integrable circuits. For qubits closer to the measurement qubit Q_1, $\overline{C}$ first decays but gradually increases for longer circuit cycles. Qubits further from Q_1 barely show any appreciate degree of OTOC decay up to 50 circuit cycles. Overall, $\overline{C}$ for different qubits converges toward values > 0.5 for the largest circuit cycles probed in this experiment. These results show how one might in some cases uses average OTOC behavior to distinguish non-integrable quantum dynamics from integrable ones.

The integrable circuits studied in Fig. S3 in fact are the digitized realizations of the so-called XY model [47] which is of wide interest in condensed-matter physics due to its ability to capture a variety of interesting physical phenomena
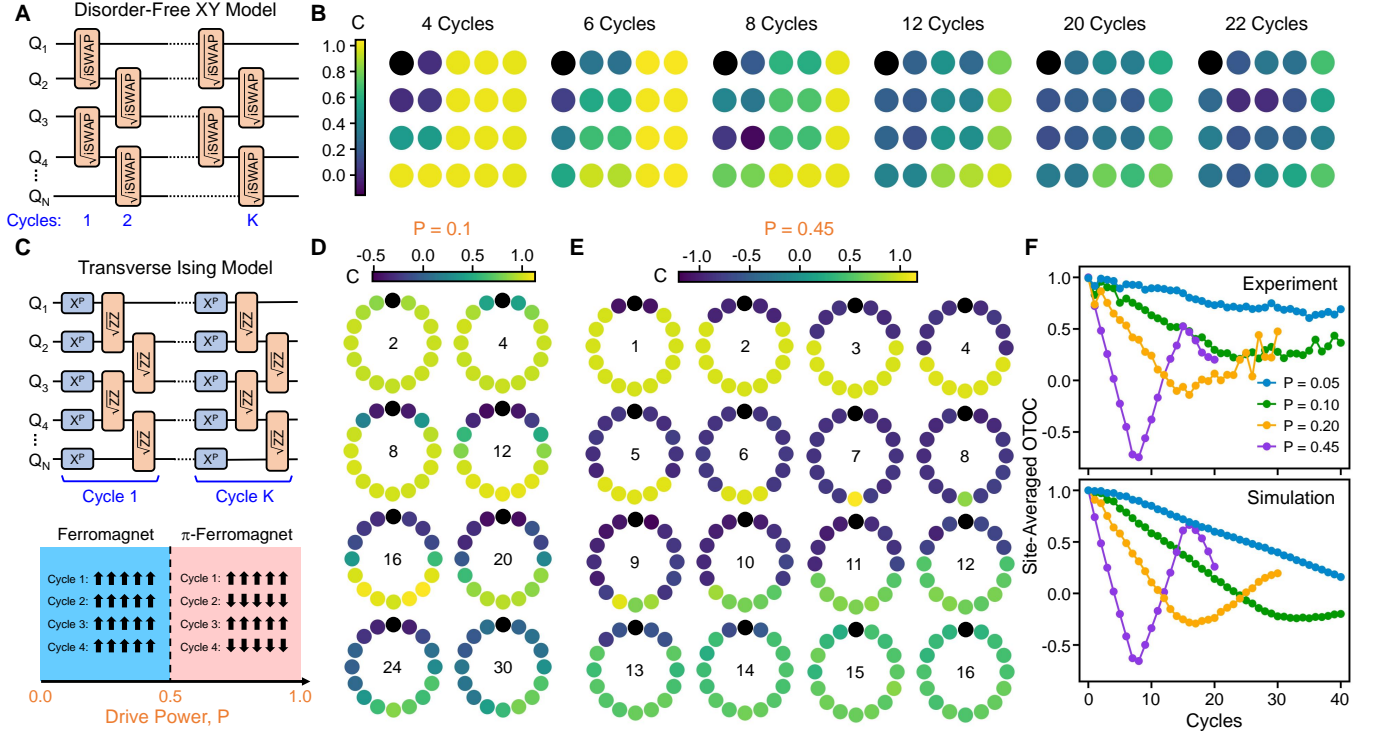
FIG. S5. OTOCs of Floquet Circuits. (A) Circuit realization of a disorder-free XY model: Each circuit cycle includes $\sqrt{\text{iSWAP}}$ gates only. (B) Cycle-dependent OTOC values, C, measured on a 2D grid of 20 qubits subject to the circuit in (A). Black filled circle denotes the location of Q_1. The ancilla qubit Q_a is omitted for simplicity. (C) Top panel: Circuit realization of a Floquet transverse Ising model. Each circuit layer includes an X rotation for every qubit with an angle πP, followed by two layers of $\sqrt{ZZ}$ gates between all nearest neighbors on a 1D chain of qubits. Bottom panel: Illustration of two dynamical phases supported by this circuit. The arrows indicate local polarization of each qubit at successive cycles. (D) Cycle-dependent OTOC values C, measured on a 1D ring of 16 qubits, subject to the circuit in (C) with $P = 0.1$. Black filled circle denotes the location of Q_1. (E) Cycle-dependent C measured with $P = 0.45$. (F) Cycle-dependent OTOC values after averaging over all qubit sites, plotted for 4 different values of P. Top panel shows experimental data and bottom panel shows exact simulation results.

such as quantum phase transitions. To demonstrate an immediate application of our work, we use OTOCs to study a particular feature of the XY-model, namely the transition from integrability to non-integrability due to geometry.

It is well-known that XY-model in 1D exhibits integrable dynamics, as demonstrated in Fig. S3. Dynamics for XY-model in 2D remains a highly active area of research and is generally non-integrable. In Fig. S4, we show that the transition into non-integrability for XY-model occurs as soon as the geometry changes from 1D to a ladder-like geometry (Fig. S4A). Here we have arranged 16 qubits into two parallel chains of 8 qubits and connected them with 5 "cross-links". Next, we measure OTOCs of random circuits implemented with this new geometry where the single-qubit gates are again randomly chosen from Z gates with angles in the interval $[-\pi, \pi]$ and the two-qubit gates are $\sqrt{\text{iSWAP}}$. The order for applying the $\sqrt{\text{iSWAP}}$ gates is shown in Fig. S4B.

The average OTOCs for this ladder-geometry XY model are shown in Fig. S4C. It is seen that the wavelike propagation and long-time limits of $\overline{C} = 0$ characteristic of non-integrable quantum circuits are both recovered in this modified geometry, indicating a transition from integrability to non-integrability for the XY-model. Detailed experimental studies of this transition with larger numbers of qubits is a subject of future work.

C.   OTOCs for Circuits with Fixed Structures

Although the main text focuses on random circuit models due to the flexibility of controlling their degrees of scrambling, the measurement scheme and error-mitigation techniques demonstrated by this work are not restricted to such circuits. Here, we show that the OTOCs of quantum circuits with fixed structures may be measured by our protocol as well.

The first of such "structured" circuits we explore is shown in Fig. S5A. Here, each circuit cycle applies $\sqrt{\text{iSWAP}}$
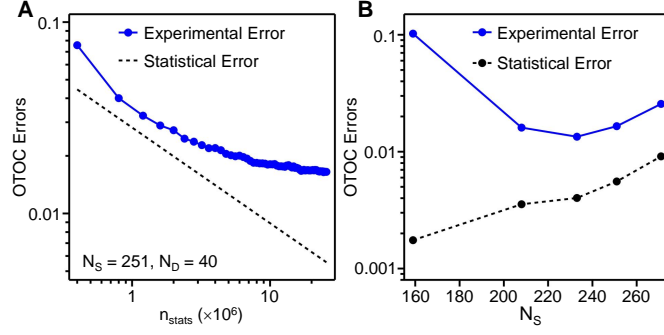
FIG. S6. Contribution of finite sampling to experimental OTOC error. (A) Dependence of experimental OTOC error on the number of single-shots used to estimate $\langle \hat{\sigma}_y \rangle$, n_{stats}. The dashed line shows expected statistical errors for different values of n_{stats}. Here the number of iSWAPs is $N_S = 251$ and the number of non-Cliffords is $N_D = 40$. (B) Comparison of experimental OTOC errors and expected statistical errors for different values of N_S. The experimental errors are reproduced from Fig. 4C of the main text. The statistical errors are calculated based on n_{stats} and the average normalization value for each N_S.

between neighboring qubits, without any random single-qubit gates. Physically, the quantum circuit corresponds to a discretized simulation of the disorder-free XY model [41]. In Fig. S5B, the spatial distribution of OTOC values C for this circuit is measured for different circuit cycles on a 2D grid of 20 qubits. Similar to the other 2D systems studied in this work, we observe clear operator spreading as evidenced by the decay of OTOCs over time. For each circuit cycle, the spatial distribution of C also assumes a diffusive profile similar to those shown in Fig. 2B of the main text.

The second circuit type we probe is illustrated in Fig. S5C. Here the circuit structure is periodic, with each cycle consisting of one layer of single-qubit gates and two layers of two-qubit gates. The single-qubit gates enact a rotation around the x-axis of the Bloch sphere with a fixed angle πP for all qubits. The two layers of $\sqrt{ZZ} = e^{-i\frac{\pi}{4}\hat{\sigma}_z^{(i)}\hat{\sigma}_z^{(i+1)}}$ gates allow all nearest-neighbor qubits (placed in 1D for this example) to interact once, where i and $i + 1$ denote the indices of two neighboring qubits. This circuit corresponds to a Floquet transverse Ising model, since the unitary for each cycle is equal to $e^{-iP\frac{\pi}{2}\sum_i \hat{\sigma}_x^{(i)}} e^{-i\frac{\pi}{4}\sum_i \hat{\sigma}_z^{(i)}\hat{\sigma}_z^{(i+1)}}$. The circuit model supports two dynamical quantum phases which are illustrated in the bottom panel of Fig. S5C: For $P \ll 0.5$, the local projections of qubits ("magnetizations") remain approximately the same as the initial state of the system over time, similar to a ferromagnet. For $P \gg 0.5$, the magnetizations change sign after each circuit cycle, a phase referred to as a π-ferromagnet [48, 49]. Close to $P \approx 0.5$, the system undergoes a phase transition.

In Fig. S5D and Fig. S5E, experimentally obtained OTOC values for the Floquet transverse Ising model are plotted for $P = 0.1$ and $P = 0.45$, respectively. Here we have used 16 qubits arranged in a ring geometry. We observe very different OTOC behaviors: Away from the phase transition ($P = 0.1$), the dynamics is slow and requires over 20 cycles before a decay in OTOC is detected for every qubit. On the other hand, the dynamics is much faster close to the phase transition ($P = 0.45$), where we see the propagation of OTOC acts like a damped travelling wave, inducing a large but increasingly weaker change in the OTOC values for the qubits at the "front" of the wave. The time-dependent OTOC values, averaged over all qubit sites, are also plotted in Fig. S5F and in good agreement with exact simulation results. We note that the observed faster spreading and larger OTOC fluctuation as the Floquet system approaches the dynamical phase transition are also in agreement with recent numerical works on similar models [50].

D. Characterization of Experimental Errors

In this section, we present additional characterization data to further corroborate and understand the experimental results in Fig. 4 of the main text. In particular, we focus on answering two questions: 1. What fraction of the observed experimental errors can be attributed to statistical errors due to limited sampling? 2. How sensitive is the signal-to-noise ratio to the number of non-Cliffords in the circuits?

We first address question 1. The role of finite sampling in experimental OTOC measurement may be understood as follows: For n_{stats} single-shot measurements, an average error of $\frac{1}{\sqrt{n_{\text{stats}}}}$ is expected to be present in the estimate for $\langle \hat{\sigma}_y \rangle$ of the ancilla qubit due to statistical uncertainty. In the presence of circuit errors and a normalization value $\langle \hat{\sigma}_y \rangle_I < 1$, this expected statistical error is amplified to a value of $\frac{1}{\langle \hat{\sigma}_y \rangle_I \sqrt{n_{\text{stats}}}}$, assuming the ideal OTOC value to be significantly smaller than 1 (i.e. $\langle \hat{\sigma}_y \rangle_I \gg |\langle \hat{\sigma}_y \rangle_B|$ where $\langle \hat{\sigma}_y \rangle_B$ is $\langle \hat{\sigma}_y \rangle$ measured with the butterfly operator applied).

In Fig. S6A, this expected statistical error is plotted as a function of n_{stats} for $N_S = 251$ and $N_D = 40$ where $\langle \hat{\sigma}_y \rangle_I \approx 0.04$. On the same plot, we have included experimental OTOC errors (i.e. the RMS deviation between
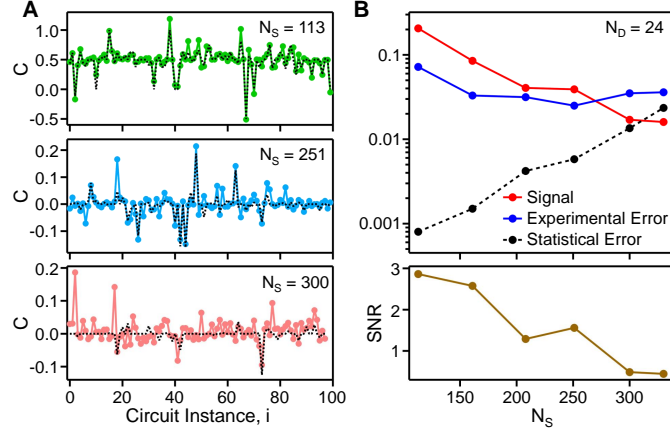
FIG. S7. OTOC errors for $N_D = 24$. (A) OTOCs of 100 random circuit instances, C, for different values of N_S. $N_D = 24$ for all circuits. The dashed lines are exact numerical simulation results using the branching method. (B) Upper panel: OTOC signal size, experimental error and estimated statistical error as functions of N_S. $N_D = 24$ for all data included here. Lower panel: SNR (i.e. ratio of OTOC signal size to experimental error) as a function of N_S.

simulated and experimental OTOC values of 100 random circuits) obtained from reduced amounts of single-shot data. We observe that the experimental error initial decreases with increasing values of n_{stats}, suggesting that statistical uncertainty being a significant source of error for small numbers of single-shot measurements. At $n_{stats} > 10^7$, the experimental error has a significantly weaker dependence on n_{stats} and is markedly higher than the expected statistical error, indicating other error sources are dominant in this regime. In Fig. S6B, we have re-plotted the experimental errors in Fig. 4C of the main text along with the expected statistical errors calculated from n_{stats} and $\langle \hat{\sigma}_y \rangle_I$ of each N_S. The increase in statistical error at higher N_S is a result of decreasing normalization values. It is evident that the observed experimental errors are consistently larger than the expected statistical errors, indicating other error mechanisms are dominant. In Section VI, we provide numerical simulation results to further analyze the sources of experimental error.

Next, we focus on the scaling of experimental error vs number of iSWAPs for a different number of non-Cliffords in the quantum circuits. Fig. S7A shows C of 100 circuit instances for $N_S = 113$, 251 and 300, all of which have $N_D = 24$. On the same plots, exactly simulated OTOC values using the branching method (Section IV) are also plotted. Similar to Fig. 4B of the main text, we observe that the agreement between experimental and simulated OTOC values degrades as N_S increases. In addition, the OTOC signal size (i.e. the fluctuation of the simulated OTOC values) also decreases as N_S increases.

In Fig. S7B, the OTOC signal size, experimental error and expected statistical error are plotted as functions of N_S (all with $N_D = 24$). Here we see that the OTOC signal size indeed monotonically decreases as N_S increases. The experimental error, on the other hand, shows less dramatic changes as a function of N_S. After taking the ratio of the OTOC signal size and the experiment error, we plot the resulting SNR as a function of N_S in the lower panel of Fig. S7B. The scaling of SNR vs N_S is roughly consistent with Fig. 4 of the main text where higher values of N_D (64 and 40) are used. In particularly, SNR falls below 1 after N_S has increased beyond ∼250. The relative insensitivity of SNR to N_D allows us to conveniently benchmark our system at lower values of N_D where classical simulation is easy. This is especially important in the future when we conduct experiments with $N_S > 400$ where tensor-contraction may no longer be feasible (Section III).

II.   EXPERIMENTAL TECHNIQUES

In this section, we describe the calibration process and metrology of quantum gates used in the OTOC experiment. In addition, we also demonstrate a series of error-mitigation strategies used in the compilation of experimental circuits which significantly reduced errors from various sources such as those related to state preparation and readout (SPAM), cross-talk, or coherent control errors on two-qubit gates.
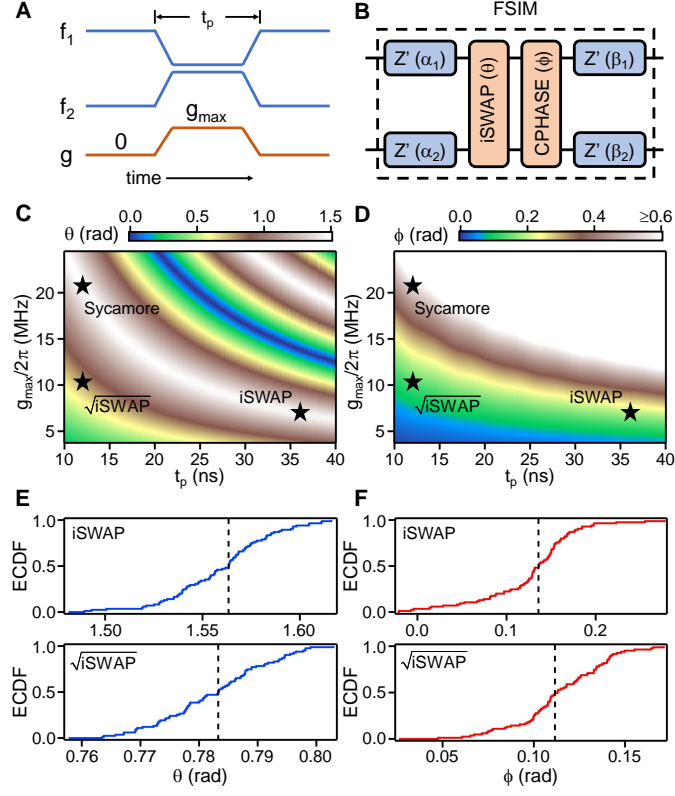
FIG. S8. Calibrating "textbook" gates. (A) Schematic illustration of the waveforms used to realize pure iSWAP and $\sqrt{\text{iSWAP}}$ gates: The $|0\rangle \to |1\rangle$ transition frequencies of two transmon qubits, f_1 and f_2, are brought close to each other by adjusting the control fluxes to their superconducting quantum interference device (SQUID) loop. Concurrently, a pulse to the coupler's SQUID flux changes the qubit-qubit coupling g from 0 to a maximum value of g_{max}. The total length of the pulses is t_{p}. (B) The generic FSIM gate realized by the waveforms in (A), composed of a partial-iSWAP gate with swap angle θ, a CPHASE gate with a conditional-phase ϕ and four local Z-rotations with angles α_1, α_2, β_1, β_2 each. (C, D) Simulated θ (C) and ϕ (D) as functions of g_{max} and t_{p}. The simulation assumes an average qubit frequency $\frac{1}{2}(f_1 + f_2) = 6.0$ GHz and an anharmonicity of 200 MHz for each transmon qubit. The operating points for three different gates, Sycamore, iSWAP and $\sqrt{\text{iSWAP}}$, are indicated by the the star symbols. (E, F) Integrated histogram (empirical cumulative distribution function, ECDF) of θ (E) and ϕ (F) for both the iSWAP and $\sqrt{\text{iSWAP}}$ gates. The data include all 86 qubit pairs on the processor. The x-axis location of each dashed line indicates the median value of the corresponding angle.

A. Calibration of iSWAP and $\sqrt{\text{iSWAP}}$ Gates

The measurement of OTOCs requires faithful inversion of a given quantum circuit, $\hat{U}$. The "Sycamore" gate used in our previous work [38], equivalent to an iSWAP gate followed by a CPHASE gate with a conditional-phase of $\pi/6$ radians (rad), is an ill-suited building block for $\hat{U}$ since its inversion cannot be easily created by combining Sycamore with single-qubit gates. On the other hand, iSWAP and $\sqrt{\text{iSWAP}}$ are commonly used two-qubit gates that can be readily inverted by adding local Z rotations:

$$G^{-1} = Z_1\left(\frac{\pi}{2}\right) Z_2\left(-\frac{\pi}{2}\right) G Z_1\left(-\frac{\pi}{2}\right) Z_2\left(\frac{\pi}{2}\right) \tag{S1}$$

Here G is the two-qubit unitary corresponding to iSWAP or $\sqrt{\text{iSWAP}}$ and $Z_i(\varphi) = e^{-i\frac{\varphi}{2}\hat{\sigma}_z^{(i)}}$, where $\hat{\sigma}_z^{(i)}$ is the Pauli-Z matrix acting on qubit i ($i = 1$ or 2). Compared to Sycamore, realizing pure iSWAP and $\sqrt{\text{iSWAP}}$ gates requires the development of two additional capabilities on our quantum processor: 1. A significant reduction of the coherent error associated with the conditional-phase in Sycamore. 2. The ability to implement arbitrary single-qubit rotations around the Z axis.

1. Reducing Conditional-Phase Errors

We first describe the calibration technique for reducing conditional phase errors. As discussed in previous works [38], such a phase arises from the dispersive interaction between the $|11\rangle$ and $|02\rangle$ (or $|20\rangle$) states of two transmon qubits while their coupling strength g is raised to a finite value to enable a resonant interaction between the $|10\rangle$ and $|01\rangle$ states (Fig. S8A). Although eliminating this phase is possible by concatenating a Sycamore gate with a pure CPHASE gate having an opposite conditional-phase [51], this process would involve complicated waveforms and large qubit frequency excursions which are demanding to implement on a 53-qubit processor. Instead, we adopt an alternative approach based on the relatively simple control waveform used in Ref. [38] (Fig. S8A). This waveform sequence produces a Fermionic Simulation (FSIM) gate comprising a partial-iSWAP gate with swap angle θ, a CPHASE gate with conditional-phase ϕ and four local Z-rotations (Fig. S8B).

Next, we consider how the angles θ and ϕ depend on readily tunable waveform parameters such as the pulse duration t_p and maximum qubit-qubit coupling g_max. This is done by numerically solving the time-evolution of two coupled transmons with typical device parameters. The dependences of θ and ϕ on t_p and g_max are shown in Fig. S8C and Fig. S8D, respectively. We observe that although both θ and ϕ increase linearly with t_p, their scaling with respect to g_max is different: $\theta \propto g_\mathrm{max}$ whereas $\phi \propto g_\mathrm{max}^2$. For a given value of θ, it is therefore possible to reduce ϕ by increasing t_p and decreasing g_max while keeping $t_\mathrm{p} g_\mathrm{max}$ constant. However, since longer gate operation is more susceptible to decoherence effects such as relaxation and dephasing, it is also desirable to minimize values of t_p. As a result, we use $t_\mathrm{p} = 12$ ns, $g_\mathrm{max}/2\pi \approx 10$ MHz for calibrating the $\sqrt{\mathrm{iSWAP}}$ gate and $t_\mathrm{p} = 36$ ns, $g_\mathrm{max}/2\pi \approx 7$ MHz for calibrating the iSWAP gate. Based on the simulation results, these choices would yield values of $\theta = \pi/4$ rad, $\phi = 0.14$ rad for the $\sqrt{\mathrm{iSWAP}}$ gate and $\theta = \pi/2$ rad, $\phi = 0.19$ rad for the iSWAP gate.

The calibrated values of θ and ϕ associated with every qubit pair on the 53-qubit processor are shown in Fig. S8E and Fig. S8F, respectively. Each angle is measured via cross entropy benchmarking (XEB), similar to previous works [38, 51]. The median value of θ is 0.783 rad (standard deviation = 0.010 rad) for $\sqrt{\mathrm{iSWAP}}$ and 1.563 rad (standard deviation = 0.027 rad) for iSWAP. These median values are very close to the target values of $\pi/4 = 0.785$ rad for $\sqrt{\mathrm{iSWAP}}$ and $\pi/2 = 1.571$ rad for iSWAP. In the case of ϕ, the median value is 0.112 rad for $\sqrt{\mathrm{iSWAP}}$ (standard deviation = 0.026 rahttps://www.overleaf.com/projectd) and 0.136 rad for iSWAP (standard deviation = 0.055 rad). The median values of ϕ are close to predictions from numerical simulation and 4 to 5 times lower compared to the Sycamore gate.

The coherent error introduced by remnant values of ϕ is further reduced by adjusting other phases of a FSIM unitary $U_\mathrm{FSIM}(\theta, \phi, \Delta_+, \Delta_-, \Delta_{-,\mathrm{off}})$, defined as:

$$\begin{pmatrix} 1 & 0 & 0 & 0 \\ 0 & e^{i(\Delta_+ + \Delta_-)}\cos\theta & -ie^{i(\Delta_+ - \Delta_{-,\mathrm{off}})}\sin\theta & 0 \\ 0 & -ie^{i(\Delta_+ + \Delta_{-,\mathrm{off}})}\sin\theta & e^{i(\Delta_+ - \Delta_-)}\cos\theta & 0 \\ 0 & 0 & 0 & e^{i(2\Delta_+ - \phi)} \end{pmatrix}. \tag{S2}$$

Here Δ_+, Δ_- and $\Delta_{-,\mathrm{off}}$ are phases that can be freely adjusted by local Z-rotations. Imperfect gate calibration often results in an actual two-qubit unitary U_a that differs slightly from the target unitary U_t, leading to a Pauli error [38, 52]:

$$r_\mathrm{p} = 1 - \frac{1}{D^2}\left|\mathrm{tr}\left(U_\mathrm{a}^\dagger U_\mathrm{t}\right)\right|^2 \tag{S3}$$

Here $D = 4$ is the dimension of a two-qubit Hilbert space.

Given that our target unitaries are $U_\mathrm{t} = U_\mathrm{FSIM}(\pi/4, 0, 0, 0, 0)$ for $\sqrt{\mathrm{iSWAP}}$ and $U_\mathrm{t} = U_\mathrm{FSIM}(\pi/2, 0, 0, 0, 0)$ for iSWAP, one may naively expect that Δ_+, Δ_- and $\Delta_{-,\mathrm{off}}$ should all be set to 0 in U_a in order to minimize r_p. While this is indeed the case if $\phi = 0$ in U_a, it is not true when ϕ assumes a finite value ϕ_a in U_a. In fact, simple algebraic calculation shows that in such a case, the minimum value of r_p occurs at $(\Delta_+, \Delta_-, \Delta_{-,\mathrm{off}}) = (\phi_\mathrm{a}/2, 0, 0)$, where it is a factor of 3 smaller compared to $(\Delta_+, \Delta_-, \Delta_{-,\mathrm{off}}) = (0, 0, 0)$. By calibrating our system such that $\Delta_+ = \phi_\mathrm{a}/2$ for every qubit pair, we estimate that the median Pauli error introduced by the conditional-phase to be only 0.07 % for $\sqrt{\mathrm{iSWAP}}$ and 0.12 % for iSWAP.

2. Arbitrary Z-Rotations

We now describe the implementation of arbitrary single-qubit Z-rotations on the quantum processor. In addition to constructing the inverse gates $\sqrt{\mathrm{iSWAP}}^{-1}$ and iSWAP^{-1}, Z-rotations are also used in removing native Z-rotations
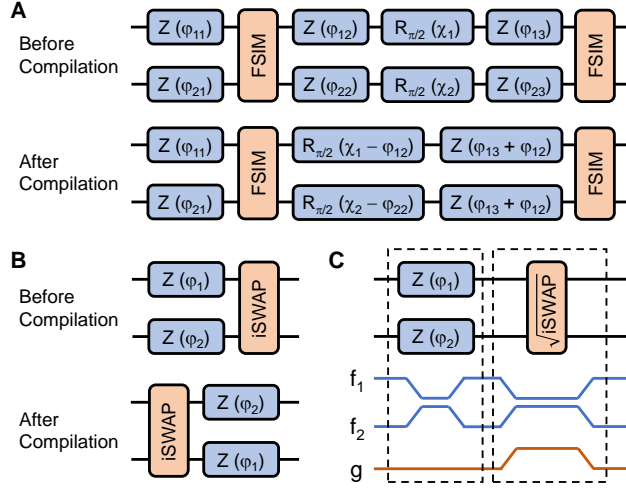
FIG. S9. Implementation of Z-rotations. (A) Circuit compilation procedure for reducing number of required Z-rotations. Z-rotations occurring after each FSIM gate are combined with the Z-rotations before the next FSIM gate. Phases on the microwave-driven single-qubit gates are shifted to maintain the same overall quantum evolution. φ_{ij} denotes the angles of various Z-rotations and χ_i denotes the phases of microwave single-qubit gates. (B) Circuit compilation procedure for pushing Z-rotations through an iSWAP gate. Combined with (A), Z-rotations in circuits containing only iSWAP and single-qubit gates become entirely virtual. (C) Schematic illustration of the waveforms used to implement Z-rotations before each $\sqrt{\text{iSWAP}}$ gate. Compared to the waveforms in Fig. S8A, an additional control flux pulse is used to detune the qubits from their idle frequencies and thereby achieve a "physical" Z-gate.

Z' in the FSIM gate (Fig. S8B) as well as adjusting values of Δ_+ to minimize conditional-phase errors. The procedure for incorporating Z-rotations into quantum circuits is two-fold: First, we recompile the circuits and combine all Z-rotations occurring after each two-qubit FSIM gate with the Z-rotations before the next FSIM gate, as shown in Fig. S9A. If any microwave-driven single-qubit gate such as $R_{\pi/2}(\chi) = e^{-i\frac{\pi}{4}(\cos\chi\hat{\sigma}_x + \sin\chi\hat{\sigma}_y)}$ occurs between the two FSIM gates, where $\hat{\sigma}_x$ and $\hat{\sigma}_y$ are Pauli-X and Pauli-Y matrices and χ is the phase of the microwave drive, we apply the equivalence $R_{\pi/2}(\chi)Z(\varphi) = Z(\varphi)R_{\pi/2}(\chi - \varphi)$ to shift the rotation axis of the single-qubit gate and "push" the Z-rotation through. This process effectively reduces the number of Z-rotations in the circuits by a factor of 2 and has been demonstrated to incur negligible degradation in the overall fidelity, since the only physical changes are modifications to the phases of the microwave drives of single-qubit gates [53].

The second step for implementing Z-rotations is different for iSWAP and $\sqrt{\text{iSWAP}}$ gates. In the case of iSWAP, the equivalence $U_{\text{FSIM}}(\pi/2, 0, 0, 0, 0)Z_1(\varphi_1)Z_2(\varphi_2) = Z_1(\varphi_2)Z_2(\varphi_1)U_{\text{FSIM}}(\pi/2, 0, 0, 0, 0)$ allows us to push Z-rotations through each two-qubit gate by simply rearranging their phases (Fig. S9B). As a result, the Z-rotations occurring in circuits with iSWAP gates are entirely virtual. In the case of $\sqrt{\text{iSWAP}}$, such equivalence does not exist and we implement Z-rotations before the two-qubit gates using additional control flux pulses, as illustrated in Fig. S9C. Here, we detune the qubit frequencies from their idle positions by an variable amount Δf and for a fixed duration $t_z = 20$ ns before each $\sqrt{\text{iSWAP}}$ gate, leading to a Z-rotation $\approx Z(2\pi\Delta f t_z)$.

B. Gate Error Benchmarking and Cross-Talk Mitigation

The Pauli errors of the calibrated iSWAP and $\sqrt{\text{iSWAP}}$ gates are measured through XEB [38, 54], which uses a collection of random circuits comprising interleaved two-qubit and random single-qubit gates. For each random circuit, the probability distribution of all possible output bit-strings is both measured experimentally and computed numerically. The statistical correlation between the two distributions ("cross-entropy") is then used to infer the total error of each quantum circuit. After measuring a sufficient number of circuit instances at different circuit depths, it has been shown that XEB reliably yields gate errors that are very consistent with values obtained from conventional characterization methods such as randomized benchmarking [13, 38, 51].

A key difference between the XEB process used in our current work compared to prior experiments [38] is the unitaries used in the numerical computation of the benchmarking circuits. Previously, such unitaries are freely adjusted for each individual qubit pair, whereby values of various FSIM angles θ, ϕ, Δ_+, Δ_- and $\Delta_{-,\text{off}}$ are optimized to obtain the lowest Pauli errors. In this work, we do not perform such an optimization step during gate error characterization
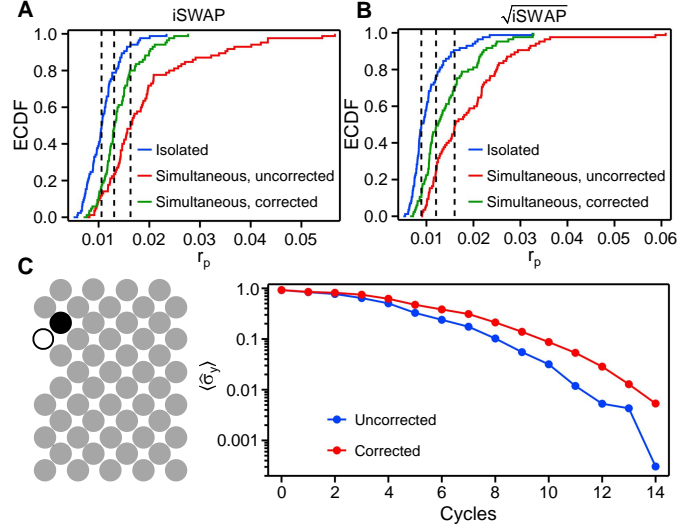
FIG. S10. Fixed-Unitary XEB and cross-talk correction. (A, B) Integrated histograms (ECDF) of Pauli errors for both the iSWAP (A) and the $\sqrt{\text{iSWAP}}$ (B) gates. Three sets of values are shown for each case: the isolated (blue) curves represent the errors obtained by operating each qubit pair individually with all other qubits at ground state. The simultaneous, uncorrected (red) curves represent the errors obtained by operating all qubits at the same time, without any additional correction. The simultaneous, corrected (green) curves represent the simultaneous error rates after additional Z-rotations are included in the circuits to offset unitary shifts induced by cross-talk effects. Simultaneous error rates are obtained from four different configurations of parallel two-qubit operations, similar to Ref. [38]. Dashed lines indicate the median locations of various errors. All error rates are obtained from XEB with pure iSWAP or $\sqrt{\text{iSWAP}}$ gate used in simulation, and include contributions from two single-qubit gates and one two-qubit gate. (C) An OTOC experimental configuration for evaluating the effects of cross-talk correction. The empty circle represents the ancilla qubit and the black filled circle represents the measurement qubit. All other qubits are represented by purple spheres. (D) The OTOC normalization value $\langle \hat{\sigma}_y \rangle$ as a function of number of cycles in a quantum circuit $\hat{U}$ for the configuration shown in (C), measured both with and without applying the cross-talk corrections. $\hat{U}$ is composed of iSWAP and random single-qubit $\pi/2$ rotations around axes on the XY plane.

and instead use a fixed unitary ($U_{\text{FSIM}}(\pi/2, 0, 0, 0, 0)$ for iSWAP and $U_{\text{FSIM}}(\pi/4, 0, 0, 0, 0)$ for $\sqrt{\text{iSWAP}}$) for all qubit pairs. The gate errors characterized by the "fixed-unitary" XEB process include contributions from both incoherent sources such as relaxation and dephasing and coherent sources such as remnant conditional-phases. The adoption of a more stringent benchmarking criterion for gate errors is motivated by the fact that both coherent and incoherent errors can lead to imperfect reversal of quantum circuits and adversely impact the accuracy of OTOC measurements, in contrast to previous experiment in which coherent errors are compensated by modifying circuits in simulation [38].

The Pauli error rate r_{p} per cycle (aggregate error of two single-qubit gates and one two-qubit gate) associated with each qubit pair is first measured in isolation. The results are plotted as integrated histograms in Fig. S10A and Fig. S10B, where we observe a mean (median) error of 0.0109 (0.0106) for iSWAP and 0.0106 (0.0089) for $\sqrt{\text{iSWAP}}$. These higher errors rates compared to our previous work [38] are a result of enhanced incoherent errors due to longer pulses used in iSWAP and additional detuning pulses in $\sqrt{\text{iSWAP}}$, as well as coherent errors arising from remnant conditional-phases.

We then repeat the same process but measure the error rates of different pairs simultaneously. We first observe, similar to previous work [38], a sizable increase in r_{p}, with the mean (median) being 0.0193 (0.0163) for iSWAP and 0.0190 (0.0161) for $\sqrt{\text{iSWAP}}$. To reduce these cross-talk effects, we first fit the XEB results to obtain the shifts in the two-qubit unitary associated with each individual qubit pair, which are often related to the single-qubit phases Δ_+, Δ_- and $\Delta_{-,\text{off}}$. In a second step, instead of simply incorporating these shifts into classical simulation as was done previously [38], we add local Z-rotations into the quantum circuits to offset the unitary shifts. The parallel error rates are then re-measured with these Z-rotations. The mean (median) value of r_{p} for simultaneous operation is reduced to 0.0140 (0.0131) for iSWAP and 0.0142 (0.0123) for $\sqrt{\text{iSWAP}}$.

The effects of the cross-talk correction can be readily seen in the "normalization" values used in the OTOC experiment. Figure S10C shows the configuration for a 53-qubit OTOC experiment. The corresponding OTOC normalization $\langle \hat{\sigma}_y \rangle$ as a function of the number of cycles in a quantum circuit is shown in Fig. S10D. Without applying the additional Z-rotations for cross-talk correction, $\langle \hat{\sigma}_y \rangle$ decays rapidly and falls below 0.1 after 8 cycles. After applying the additional Z-rotations, $\langle \hat{\sigma}_y \rangle$ decays at a visibly slower rate and falls below 0.1 after 10 cycles. The
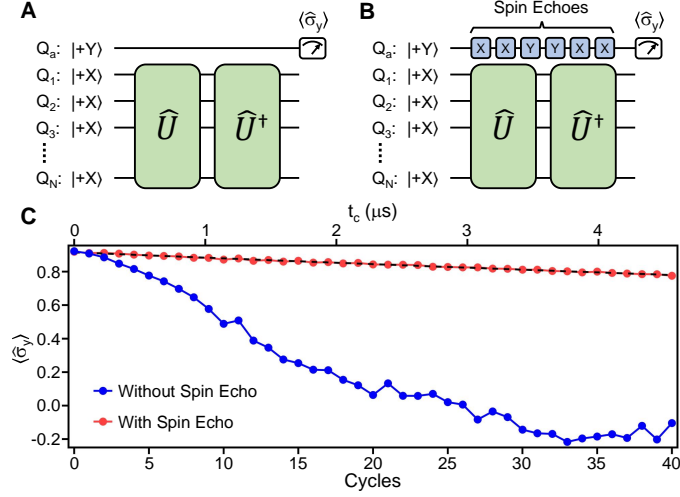
FIG. S11. Dynamical coupling in OTOC experiments. (A) Test experimental circuit for benchmarking the intrinsic coherence of the ancilla qubit. Compared to an actual OTOC circuit, the CZ gates between the ancilla qubit and measurement qubit is removed. (B) Same circuit as (A) with the additional of consecutive spin echo pulses to the ancilla qubit during the quantum circuits $\hat{U}$ and $\hat{U}^\dagger$, in the form of random X or Y gates. (C) The projection of the ancilla qubit to the y-axis, $\langle\hat{\sigma}_y\rangle$, at the end of the circuit, measured with (red) and without (blue) spin echo. The bottom x-axis of the plot shows the number of cycles in $\hat{U}$ ($\hat{U}^\dagger$ has the same number of cycles), and the top x-axis shows the corresponding total circuit duration t_c.

slower decay of $\langle\hat{\sigma}_y\rangle$ is indicative of more accurate inversion of the quantum circuit after cross-talk correction.

C. Dynamical Decoupling

We now describe a series of additional error-mitigation techniques used in the compilation of quantum circuits that further improve the accuracy of OTOC experiments. The first such technique is dynamical decoupling, motivated by long "idling" times at non-ground states for some of the qubits during the experiment. The most prominent of such qubits is the ancilla qubit, which remains idle throughout the time needed to implement the quantum circuit $\hat{U}$ and its inverse $\hat{U}^\dagger$. Intrinsic decoherence of the ancilla qubit can in principle limit the circuit depth at which OTOC can be resolved, especially if the characteristic time T_2 is comparable to the total duration of $\hat{U}$ and $\hat{U}^\dagger$.

To benchmark the intrinsic T_2 of the ancilla qubit during an OTOC experiment, we design the test circuits shown in Fig. S11A and Fig. S11B. In either case, we removed the two CZ gates otherwise present in an actual OTOC experiment such that the ancilla qubit does not interact with any other qubit apart from cross-talk effects. The difference between the two cases is that the ancilla qubit remains completely idle during $\hat{U}$ and $\hat{U}^\dagger$ in Fig. S11A, whereas a train of spin echo pulses $X - X - Y - Y - X - X...$ is applied to the ancilla qubit during $\hat{U}$ and $\hat{U}^\dagger$ in Fig. S11B.

The y-axis projection of the ancilla qubit, $\langle\hat{\sigma}_y\rangle$, at the end of $\hat{U}$ and $\hat{U}^\dagger$ is measured both with and without the added spin echoes. The results are shown in Fig. S11C. We observe that without spin echo, $\langle\hat{\sigma}_y\rangle$ decays rather quickly despite no entanglement between the ancilla and other qubits in the system, falling to ~0 after 25 circuit cycles (corresponding to an evolution time $t_c \approx 3.0$ μs). The Gaussian shape of the decay at earlier times suggests that low-frequency noise is likely the dominant source of decoherence [55]. On the hand, with the addition of spin echo, $\langle\hat{\sigma}_y\rangle$ decays at a much slower rate maintaining a value of 0.78 even after 40 circuit cycles ($t_c \approx 4.6$ μs). By fitting $\langle\hat{\sigma}_y\rangle$ to a functional form $Ae^{-\frac{t_c}{T_2}}$ where A and T_2 are fitting parameters, we obtain a coherence time $T_2 = 28.6$ μs for the ancilla qubit, which is close to the $2T_1$ limit of our quantum processor [38]. Given this value of T_2 is significantly longer than all OTOC experimental circuits used in this work (the longest circuit lasts ~5 μs), we conclude that changes in the ancilla projection $\langle\hat{\sigma}_y\rangle$ in the OTOC experiments are indeed dominated by the many-body effects in $\hat{U}$ and $\hat{U}^\dagger$ rather than the intrinsic decoherence of the ancilla qubit itself. For all experimental results presented in the main text, spin echo is applied to the ancilla qubit.
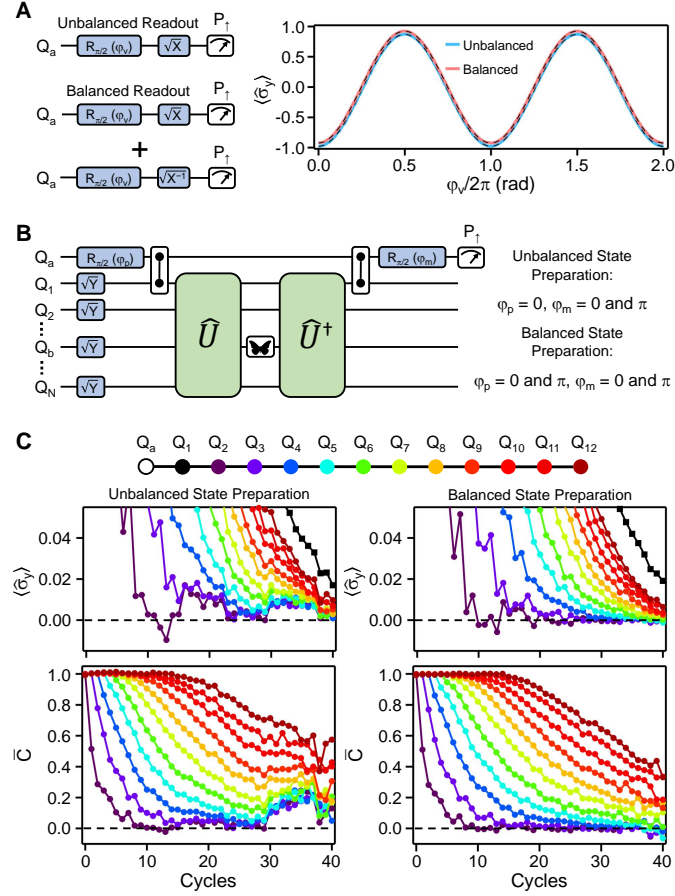
FIG. S12. Unbiased measurements of $\langle \hat{\sigma}_y \rangle$. (A) Left panel shows the test circuits for characterizing $\langle \hat{\sigma}_y \rangle$ arising from asymmetry in readout fidelities. Two different schemes are implemented. The conversion between the excited-state population(s) $P_\uparrow$ and $\langle \hat{\sigma}_y \rangle$ is described in the main text. Right panel shows the experimental values of $\langle \hat{\sigma}_y \rangle$ as a function of the variable phase φ_v, obtained with both readout schemes. Dashed lines show fits to $\langle \hat{\sigma}_y \rangle = (1 - 2F_r) \cos(\varphi_v) + d_r$, where F_r and d_r are fitting parameters. (B) Schematic of the full OTOC circuit showing two different state preparation schemes: in the unbalanced scheme, only one phase is used for the first $R_{\pi/2}$ gate on the ancilla qubit. In the balanced scheme, two different phases are used. Balanced readout is used in both schemes. (C) Results of a 12-qubit OTOC experiment. Upper panels show $\langle \hat{\sigma}_y \rangle$ at different number of circuit cycles. The black squares represent the normalization case and the colored spheres represent $\langle \hat{\sigma}_y \rangle$ obtained with the butterfly operator (Z) successively applied to qubits 2 (Q_2) through 12 (Q_{12}). The location of the butterfly operator for each curve is indicated by the color legend on top. The normalized OTOCs, $\overline{C}$, are shown in the lower panels. The data are the average values of 40 different random circuit instances.

D.   Elimination of Bias in $\langle \hat{\sigma}_y \rangle$

The accuracy of OTOC measurements is particularly susceptible to any bias in $\langle \hat{\sigma}_y \rangle$ of the ancilla qubit, i.e. a fixed offset d to the ideal value. Such a bias can, for example, be introduced by the different readout fidelities for the $|0\rangle$ and $|1\rangle$ states of the ancilla qubit. To see the impact of the bias on OTOC, we consider an ideal OTOC value of C_0 and an ideal normalization value of $\langle \hat{\sigma}_y \rangle_I$. The ideal y-projection of the ancilla with the butterfly operator applied, $\langle \hat{\sigma}_y \rangle_B$, in such a case is $\langle \hat{\sigma}_y \rangle_B \approx C_0 \langle \hat{\sigma}_y \rangle_I$. However, in the presence of a bias, the measured projections become $\langle \hat{\sigma}_y \rangle = \langle \hat{\sigma}_y \rangle_I + d$ for the normalization value and $\langle \hat{\sigma}_y \rangle = \langle \hat{\sigma}_y \rangle_B + d$ with the butterfly operator applied. The experimental value for OTOC then becomes $C_1 = \frac{\langle \hat{\sigma}_y \rangle_B + d}{\langle \hat{\sigma}_y \rangle_I + d} \approx \frac{C_0 \langle \hat{\sigma}_y \rangle_I + d}{\langle \hat{\sigma}_y \rangle_I + d}$. Assuming typical values of $\langle \hat{\sigma}_y \rangle_I = 0.05$ and $C_0 = 0.1$, even a small asymmetry $d = 0.01$ would lead to a highly erroneous value of $C_1 \approx 0.25$. It is therefore crucial to identify and mitigate any bias in $\langle \hat{\sigma}_y \rangle$ of the ancilla qubit.

We begin by measuring $\langle \hat{\sigma}_y \rangle$-bias due to asymmetry in readout errors. The test circuit is shown in the left panel of Fig. S12A under the label "unbalanced readout". We first project the qubit onto the equator of the Bloch sphere with a $\pi/2$ rotation, $R_{\pi/2}(\varphi_v)$, where φ_v is a variable phase. A second $\pi/2$ rotation around a fixed axis, $\sqrt{X}$, is then applied and excited state population $P_\uparrow$ is finally measured. The population is then converted to $\langle \hat{\sigma}_y \rangle$ via $\langle \hat{\sigma}_y \rangle = 2P_\uparrow - 1$. The

right panel of Fig. S12A shows $\langle \hat{\sigma}_y \rangle$ as a function of φ_v and a fit to a functional form $\langle \hat{\sigma}_y \rangle = (1 - 2F_r) \cos(\varphi_v) + d_r$. Here F_r is the average of the readout fidelities of the $|0\rangle$ and $|1\rangle$ states, and d_r is their difference. For this unbalanced readout scheme, we obtain $F_r = 0.0962$ and $d_r = 0.055$. The observed difference in readout fidelities is consistent with past experiments where it was shown that energy relaxation of the qubit during dispersive readout generally leads to lower readout fidelity for the $|1\rangle$ state compared to the $|0\rangle$ state [56].

The bias $d_r = 0.055$ is significantly reduced by adopting a "balanced readout" scheme, also shown in the left panel of Fig. S12A. Here, we measure the $P_\uparrow$ of the ancilla qubit with the second gate in the test circuit being either $\sqrt{X}$ or $\sqrt{-X}$. The results are then combined to obtain $\langle \hat{\sigma}_y \rangle = (P_{\uparrow,+} - P_{\uparrow,-})$, where $P_{\uparrow,\pm}$ is $P_\uparrow$ measured with the second gate being $\sqrt{\pm X}$. The averaged $\langle \hat{\sigma}_y \rangle$ is shown in the right panel of Fig. S12A as a function of φ_v. A similar fit as before yields the same average readout fidelity $F_r = 0.0962$ and a much reduced bias $d_r \approx 0.0002$.

Balanced readout alone, as we will demonstrate below, is insufficient for completely removing bias from $\langle \hat{\sigma}_y \rangle$. For all experiments reported in the main text, we apply a second symmetrization step shown in Fig. S12B, which is the measurement scheme for OTOC with the gates related to SPAM explicitly shown. Here, we parametrize both the phase φ_p of the first $\pi/2$ gate and the phase φ_m of the last $\pi/2$ gate on the ancilla qubit. In an "unbalanced state preparation" scheme, we measure the average projections $\langle \hat{\sigma}_y \rangle = (P_{\uparrow,++} - P_{\uparrow,+-})$, where $P_{\uparrow,++}$ and $P_{\uparrow,+-}$ are $P_\uparrow$ obtained with $(\varphi_p, \varphi_m) = (0, 0)$ and $(\varphi_p, \varphi_m) = (0, \pi)$, respectively. In a "balanced state preparation" scheme, we measure the average projections $\langle \hat{\sigma}_y \rangle = \frac{1}{2}(P_{\uparrow,++} - P_{\uparrow,+-} - P_{\uparrow,-+} + P_{\uparrow,--})$, where $P_{\uparrow,-+}$ and $P_{\uparrow,--}$ are additional populations obtained with $(\varphi_p, \varphi_m) = (\pi, 0)$ and $(\varphi_p, \varphi_m) = (\pi, \pi)$, respectively.

The difference between the two state preparation schemes is illustrated in Fig. S12C, where we present the results of a 12-qubit OTOC experiment. The quantum circuit $\hat{U}$ is non-integrable and composed of $\sqrt{\text{iSWAP}}$ and random single-qubit $\pi/2$ rotations around 8 different axes on the XY plane. A total of 40 circuit instances are used and the data shown are average values over all instances. The top panels show the measured values of $\langle \hat{\sigma}_y \rangle$ for the normalization case and cases where a butterfly operator Z is successively applied to qubits 2 to 12 in-between $\hat{U}$ and $\hat{U}^\dagger$. The y-axis scale is intentionally limited to < 0.05. We observe in the case of unbalanced state preparation, the $\langle \hat{\sigma}_y \rangle$ values exhibit sudden rise from 0 to >0.006 at cycles 29 to 38. This behavior is inconsistent with the effects of scrambling and decoherence, either of which is expected to lead to monotonic decay of $\langle \hat{\sigma}_y \rangle$ toward 0 for a non-integrable process. In contrast, with balanced state preparation, $\langle \hat{\sigma}_y \rangle$ indeed monotonically decays toward 0 at large cycles for all curves.

The bottom panels of Fig. S12C show the normalized average OTOCs, $\overline{C}$, for each qubit. Here we observe that $\overline{C}$ obtained with the unbalanced state preparation scheme again manifests unphysical jumps from 0 at cycles 29 to 38, resulting from the finite bias $\langle \hat{\sigma}_y \rangle$ and the mechanism outlined at the beginning of this section. In contrast, $\overline{C}$ obtained with the balanced state preparation scheme decays monotonically toward 0, in agreement with the scrambling behavior of a non-integrable process. These data suggest that a symmetrization step duration the state preparation phase of the ancilla qubit is needed to completely remove the bias in $\langle \hat{\sigma}_y \rangle$, in addition to the symmetrization step before readout. The physical origin of the remnant bias seen in the left panels of Fig. S12C is not completely understood at the time of writing, and could be related to control errors in the single-qubit gates on the ancilla qubit, incomplete depolarization of T_1 errors by the spin echoes, or other unknown mechanisms.

E. Light-cone Filter

Analogous to classical systems, quantum perturbations often travel at a limited speed (the "butterfly velocity"). This typically results in a "light-cone" structure for many quantum circuits, which can be capitalized to reduce their classical simulation costs [57]. Similarly, the light-cone structure of these quantum circuits may also be utilized to modify their implementations on a quantum processor and improve the fidelity of experimental results. In this section, we describe a light-cone-based circuit re-compilation technique that led to considerable improvements in the accuracy of experimental OTOC measurements.

Figure S13A displays the generic structure of an OTOC measurement circuit, where the component gates of the quantum circuit $\hat{U}$ and its inverse $\hat{U}^\dagger$ are explicitly shown. The butterfly operator possesses a pair of triangular light-cones extending from the middle of the circuit into both $\hat{U}$ and $\hat{U}^\dagger$. Quantum gates outside these light-cones may be completely removed ("filtered") without altering the output of the circuit. Furthermore, since the measurement at the end of the circuit is also localized at a single qubit (Q_1), one may additionally discard quantum gates outside the light-cone of Q_1 originating from the right-end of $\hat{U}^\dagger$, without altering circuit output. The gates removed by the light-cone filter are shown with semi-transparent colors in Fig. S13A. In practice, some qubits have much longer idling times as a result of gate removal and become more susceptible to decoherence effects such as relaxation and dephasing. To mitigate such effects, we also apply spin echo to qubits with long idling times, similar to the approach to the ancilla qubit in Fig. S11.

The effects of the light-cone filter on OTOC measurements are shown in Fig. S13B and Fig. S13C. The left panel
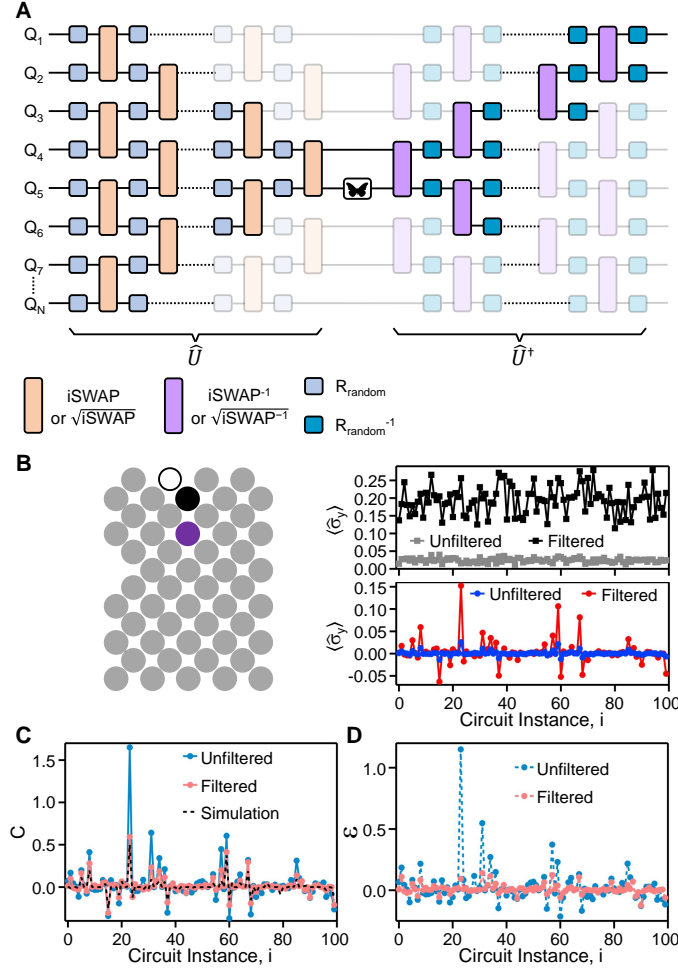
FIG. S13. Re-compiling OTOC circuits with light-cone filter. (A) Schematic of an OTOC measurement circuit, including the component gates of the quantum circuits $\hat{U}$ and $\hat{U}^\dagger$. The ancilla qubit and its related gates, as well as the $\sqrt{Y}$ gates used in the state preparation of all qubits, are omitted for simplicity. Gates shown with semi-transparent colors can be removed from the OTOC measurement circuit without altering its output. (B) Left panel shows a configuration for evaluating experimental effects of the light-cone filter. The unfilled circle represents the ancilla qubit and the black filled circle represents the measurement qubit. The purple filled circle indicates the butterfly qubit. The total number of circuit cycles is 11. Right panel shows the measured values of $\langle \hat{\sigma}_y \rangle$ for 100 random circuit instances. Data obtained in the normalization case are shown on top and data obtained with the butterfly operator applied are shown at the bottom. The same number of repetitions (1 million) is used in all cases to estimate $\langle \hat{\sigma}_y \rangle$. (C) Normalized experimental OTOC values C for different circuit instances, plotted alongside exact numerical simulation results. (D) Experimental errors ϵ for different circuit instances, corresponding to the differences between experimental and simulated values.

of Fig. S13B shows the configuration for a 53-qubit OTOC experiment. Here we choose a quantum circuit $\hat{U}$ with iSWAP and random single-qubit gates which are $\pi/2$ rotations around axes on the XY plane. The axes of rotation are chosen such that exactly 48 non-Clifford rotations (randomly selected from $\sqrt{\pm W}$ and $\sqrt{\pm V}$) occur in $\hat{U}$ and $\hat{U}^\dagger$. All other single-qubit gates are Clifford rotations randomly selected from $\sqrt{\pm X}$ and $\sqrt{\pm Y}$). The number of circuit cycles is fixed at 11. The right panels of Fig. S13B show experimental results for 100 individual instances of $\hat{U}$, whereby $\langle \hat{\sigma}_y \rangle$ for the normalization case is plotted at the top and $\langle \hat{\sigma}_y \rangle$ with the butterfly operator (X) applied is plotted at the bottom. We observe significant enhancements in the amplitudes of $\langle \hat{\sigma}_y \rangle$ after the application of the light-cone filter, with the normalization $\langle \hat{\sigma}_y \rangle$ values averaging to 0.024 without the filter and 0.194 with filter.

The experimental improvement facilitated by the light-cone filter is more clearly seen by comparing the normalized OTOC values C with exact numerical simulation of the same circuits, as shown in Fig. S13C. Without the light-cone filter, the experimental C values are substantially different from simulation results. On the other hand, with the light-cone filter, the agreement between experimental and simulated values is much closer. We further quantify the effect of light-cone filter by plotting the differences between numerical and experimental values of C, ϵ, in Fig. S13D.
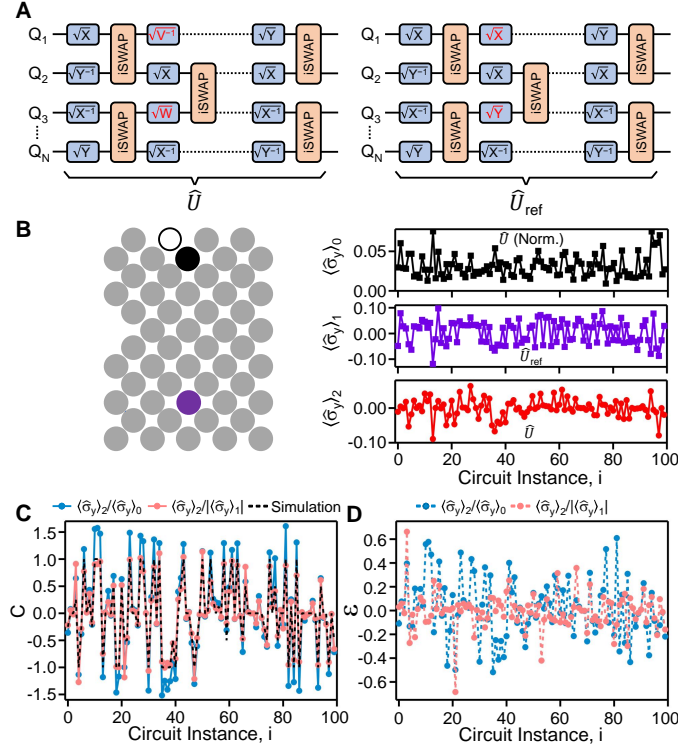
FIG. S14. Normalization via reference Clifford circuits. (A) Schematic of two quantum circuits: $\hat{U}$ is the actual quantum circuit of interest, composed mostly of Clifford gates and a few non-Clifford gates ($\sqrt{\pm V}$ and $\sqrt{\pm W}$). $\hat{U}_{\mathrm{ref}}$ is a reference circuit with the same Clifford gates as $\hat{U}$. The non-Clifford gates in $\hat{U}$ are replaced with random Clifford gates $\sqrt{\pm X}$ and $\sqrt{\pm Y}$ in $\hat{U}_{\mathrm{ref}}$. (B) Left panel shows an experimental configuration for comparing two normalization procedures. The black unfilled (filled) circle represents the ancilla (measurement) qubit. The purple filled circle represents the butterfly qubit. The total number of circuit cycles is 14. Right panel shows the measured values of $\langle\hat{\sigma}_{\mathrm{y}}\rangle$ for 100 random circuit instances. $\langle\hat{\sigma}_{\mathrm{y}}\rangle_0$ denotes values obtained without applying butterfly operator to $\hat{U}$, $\langle\hat{\sigma}_{\mathrm{y}}\rangle_1$ denotes values obtained with butterfly operator applied to $\hat{U}_{\mathrm{ref}}$, and $\langle\hat{\sigma}_{\mathrm{y}}\rangle_2$ denotes values obtained with butterfly operator applied to $\hat{U}$. The same number of repetitions (4 millions) is used in all cases to estimate $\langle\hat{\sigma}_{\mathrm{y}}\rangle$. (C) Normalized experimental OTOC values C for different circuit instances, plotted alongside exact numerical simulation results. (D) Experimental errors ϵ for different circuit instances, corresponding to the differences between experimental and simulated values.

Here we observe that the root-mean-square (RMS) value for ϵ is 0.156 without the light-cone filter, whereas it is reduced to 0.041 after filter is applied. This four-fold improvement in accuracy of OTOC measurements is a natural consequence of the reduction of number of gates in the overall quantum circuit (the number of iSWAP gates is reduced from 464 to 161 for the example in Fig. S13). Although the additional qubit idling introduced by the light-cone filter carries errors as well, they are expected to be much less than the errors of the removed two-qubit gates, particularly when spin echo is also applied during the idling.

F.   Normalization via Reference Clifford Circuits

The last error-mitigation technique we use for the OTOC experiment is specific to quantum circuits $\hat{U}$ composed of predominantly Clifford gates with a small number of non-Clifford gates. For such circuits, it is found through numerical studies that a modified normalization procedure yields more accurate values of OTOC (Fig. S14A): Consider a quantum circuit $\hat{U}$ composed of mostly Clifford gates (iSWAP, $\sqrt{\pm X}$ and $\sqrt{\pm Y}$) and a small number of non-Clifford gates ($\sqrt{\pm V}$ and $\sqrt{\pm W}$). We first measure the $\langle\hat{\sigma}_{\mathrm{y}}\rangle$ of the ancilla with a butterfly operator applied between $\hat{U}$ and $\hat{U}^{\dagger}$ (we denote this value as $\langle\hat{\sigma}_{\mathrm{y}}\rangle_2$), same as before. In a second step, instead of measuring $\langle\hat{\sigma}_{\mathrm{y}}\rangle$ without applying the butterfly operator (denoted by $\langle\hat{\sigma}_{\mathrm{y}}\rangle_0$), we measure $\langle\hat{\sigma}_{\mathrm{y}}\rangle$ with the same butterfly operator but a different quantum circuit $\hat{U}_{\mathrm{ref}}$ and its inverse $\hat{U}_{\mathrm{ref}}^{\dagger}$ (denoted by $\langle\hat{\sigma}_{\mathrm{y}}\rangle_1$). The reference circuit $\hat{U}_{\mathrm{ref}}$ has the same Clifford gates as $\hat{U}$, whereas the non-Clifford gates in $\hat{U}$ are replaced with Clifford gates chosen randomly from $\sqrt{\pm X}$ and $\sqrt{\pm Y}$.

Example data showing $\langle \hat{\sigma}_\text{y} \rangle_1$, $\langle \hat{\sigma}_\text{y} \rangle_2$ and $\langle \hat{\sigma}_\text{y} \rangle_3$ are shown in Fig. S14B, where $\hat{U}$ contains a total of 8 non-Clifford rotations and 14 cycles. Similar to the previous section, we present results from 100 circuit instances. Next, we process the data to obtain experimental values of OTOC, C, in two different ways: First, we apply $C = \langle \hat{\sigma}_\text{y} \rangle_2 / \langle \hat{\sigma}_\text{y} \rangle_0$, which corresponds to the normalization procedure used in the previous sections. Second, we apply $C = \langle \hat{\sigma}_\text{y} \rangle_2 / \left| \langle \hat{\sigma}_\text{y} \rangle_1 \right|$, corresponding to normalization using $\langle \hat{\sigma}_\text{y} \rangle$ of a reference circuit. Here the absolute sign accounts for the fact that the theoretical OTOC values of Clifford circuits are ± 1. The resulting C values are both plotted alongside exact simulation results in the left panel of Fig. S14C. It is easily seen that the second normalization procedure with reference Clifford circuits yields experimental values that are in much better agreement with simulation results. Indeed, the experimental errors ϵ (Fig. S14D) have an RMS value of 0.250 when $C = \langle \hat{\sigma}_\text{y} \rangle_2 / \langle \hat{\sigma}_\text{y} \rangle_0$ is used and 0.157 when $C = \langle \hat{\sigma}_\text{y} \rangle_2 / \left| \langle \hat{\sigma}_\text{y} \rangle_1 \right|$ is used. Given these observations, we adopt normalization via reference Clifford circuits when measuring quantum circuits dominated by Clifford gates.

Lastly, we note that for the data in Fig. 3 and Fig. 4 of the main text, we apply a ensemble of reference circuits $\hat{U}_\text{ref}$ and use the average value of $|\langle \hat{\sigma}_\text{y} \rangle|$ obtained from all $\hat{U}_\text{ref}$ to normalize $\langle \hat{\sigma}_\text{y} \rangle$ of the actual quantum circuit $\hat{U}$. The typical number of $\hat{U}_\text{ref}$ for each $\hat{U}$ is 10 in Fig. 3 and varies between 15 and 70 for Fig. 4.

III.   LARGE-SCALE SIMULATION OF OTOCS OF INDIVIDUAL CIRCUITS

In the last few years, there has been a constant development of new numerical techniques to simulate large scale quantum circuits. Among the many promising methods, two major numerical techniques are widely used on HPC clusters for large scale simulations: tensor contraction [40, 58–62] and Clifford gate expansion [37, 63–65]. All the aforementioned methods have advantages and disadvantages, which mainly depend on the underlying layout of the quantum circuits and the type of used gates. On the one hand, tensor contraction works best for shallow circuits with a small treewidth [62, 66]. On the other hand, Clifford gate expansion is mainly used to simulate arbitrary circuit layouts with few non-Clifford gates. Indeed, it is well known that circuits composed of Clifford gates only can be simulated in polynomial time [37], with a numerical cost which grows exponentially with the number of non-Clifford gates [63]. Both methods can be used to sample exact and approximate amplitudes, with a computational cost which decreases with an increasing level of noise. For instance, approximate amplitudes can be sampled by slicing large tensor network and contracting only a fraction of the resulting sliced tensors [67, 68]. The final fidelity of the sample amplitudes is therefore proportional to the fraction of contracted slices [60, 61], which can be tuned to match experimental fidelity. Similarly, it is possible to sample approximate amplitudes by only selecting the dominant stabilizer states in the Clifford expansion [64, 65].

In our numerical simulations, we used tensor contraction to compute approximate OTOC values, which are then validated using results from the Clifford expansion for circuits with a small number of non-Clifford gates. Both methods are described in the following sections.

A.   Numerical Calculation of the OTOC Value

As described in the main text and shown in Fig. 1(A), the experimental OTOC circuits have density-matrix-like structure of the form

$$\hat{C} = \hat{U}^\dagger \, \hat{\sigma}^{(Q_b)} \, \hat{U}, \tag{S4}$$

with $\hat{\sigma}^{(Q_b)}$ being the butterfly operator. In all numerical simulations, we used iSWAPs as entangling two-qubit gates. Before and after $\hat{C}$, a controlled-Z gate is applied between the qubit Q_1 (in $\hat{C}$) and an ancilla qubit Q_a (external to $\hat{C}$): the OTOC value is therefore obtained by computing the expectation value of $\langle \hat{\sigma}_y \rangle$ relative to the ancilla qubit Q_a. To reduce the computational cost, it is always possible to project the ancilla to either 0 or 1 (in the computational basis). Let us call $\hat{C}_0 = \hat{C}$ ($\hat{C}_1 = \hat{\sigma}_z^{(Q_1)} \hat{C} \, \hat{\sigma}_z^{(Q_1)}$) the circuit with the ancilla qubit projected on 0 (1). Therefore, the OTOC value $\langle \hat{\sigma}_y \rangle$ can be obtained as:

$$\langle \hat{\sigma}_y \rangle = \mathbb{R} \left[\langle \psi_1 | \psi_0 \rangle \right], \tag{S5}$$

with $|\psi_0\rangle = \hat{C}_0 |+\rangle$ and $|\psi_1\rangle = \hat{C}_1 |+\rangle$ respectively.

B. Branching Method

To get exact OTOC value for circuit with a small number of non-Clifford rotations, we used a branching method based on the Clifford expansion. More precisely, recalling that OTOC circuits have a density-matrix-like structure, that is $\hat{C} = \hat{U}^\dagger \hat{\sigma}^{(Q_b)} \hat{U} = \left(\hat{g}_t^\dagger \cdots \hat{g}_1^\dagger\right) \hat{\sigma}^{(Q_b)} \left(\hat{g}_1 \cdots \hat{g}_t\right)$, it is possible to apply each pair of gates $\left\{\hat{g}_t, \hat{g}_t^\dagger\right\}$ to $\hat{\sigma}^{(Q_b)}$ iteratively and "branch" only for non-Clifford gates.

At the beginning of the simulation, a Pauli "string" is initialized to all identities except a $\hat{\sigma}_x^{(Q_b)}$ operator (the butterfly operator) on the butterfly qubit Q_b (in this examples, the Pauli X is chosen as butterfly operator), that is $\mathcal{P} = \hat{I}^{(1)} \hat{I}^{(2)} \cdots \hat{\sigma}_x^{(Q_b)} \cdots$. Whenever a pair of Clifford operators $\left\{\hat{g}_t, \hat{g}_t^\dagger\right\}$ is applied to $\mathcal{P}$, the Pauli string is "evolved" to another Pauli string. For instance, an iSWAP operator evolves the Pauli string $\mathcal{P} = \hat{I} \, \hat{\sigma}_x$ to $\mathcal{P}' =$ iSWAP$^\dagger \left(\hat{I} \, \hat{\sigma}_x\right)$ iSWAP $= -\hat{\sigma}_y \hat{\sigma}_z$. On the contrary, if a non-Clifford operator is applied to $\mathcal{P}$, the Pauli string $\mathcal{P}$ will evolve into a superposition of multiple Pauli strings, that can be eventually explored as independent branches. As an example, the non-Clifford rotation $\hat{g}_t = \sqrt{W} = \sqrt{X + Y}$ will branch $\mathcal{P} = \hat{\sigma}_x$ three times into $\mathcal{P}'_1 = \frac{\hat{\sigma}_x}{\sqrt{2}}$, $\mathcal{P}'_2 = \frac{\hat{\sigma}_y}{\sqrt{2}}$ and $\mathcal{P}'_3 = \frac{\hat{\sigma}_z}{2}$ respectively. Because $\left\{\hat{g}_t, \hat{g}_t^\dagger\right\}$ are always applied in pairs (one gate from U and one gate from $U^\dagger$), the computational complexity depends on the number N_D of non-Clifford gates in U only (U and $U^\dagger$ may have a different number of non-Cliffords because of the different lightcones acting on them. See Fig. S13A). More precisely, our branching algorithms scales as the number of branches n_b induced by the N_D non-Clifford rotations in U, that is $\mathcal{O}\left(n_b\right)$.

After the applications of all $\{\hat{g}_i\}_{i=1,\ldots,t}$ gates, the OTOC circuit $\hat{C}$ will be then represented as a superposition of distinct Pauli strings, each with a different amplitude. The full states $|\psi_0\rangle$ and $|\psi_1\rangle$ can be then obtained by applying the initial state $|+\rangle$ to the Clifford expansion of $\hat{C}$ and, therefore, the OTOC value from Eq. (S5). To reduce the memory footprint of our branching method, the initial state $|+\rangle$ is always applied to all Pauli strings once the last gate in U is applied. Therefore, our branching algorithm will output both $|\psi_0\rangle$ and $|\psi_1\rangle$ as a superposition of binary strings. Because some of binary string composing $|\psi_0\rangle$ and $|\psi_1\rangle$ may have a zero amplitude, (due to destructive interference), the number of binary strings n_p composing $|\psi_0\rangle$ and $|\psi_1\rangle$ is typically smaller than the number of explored branches n_b, that is $n_p \leq n_b$.

Fig S15 (top) shows the number of explored branches n_b by varying the number N_D of non-Clifford rotations in $\hat{U}$. Because the only non-Clifford gates used in the OTOC experimental circuits are $\sqrt{W^\pm}$ and $\sqrt{V^\pm}$, with $W = X + Y$ and $V = X - Y$ respectively, one can compute the expected scaling by assuming that, at each branching point, there is an homogeneous probability to find any of the four Pauli operators $\{I, X, Y, Z\}$. Because non-Clifford rotations branch only twice on Z, thrice on $\{X, Y\}$ and never on I, the expected scaling is $n_b \propto 3^{\frac{n}{2}} 2^{\frac{n}{4}}$, which has been confirmed numerically in Fig. S15 (top). Fig S15 (bottom) shows the runtime (in seconds) to explore a given number of branches on single nodes of the NASA cluster Merope [69]. While the interface of our branch simulator is completely written in Python, the core part is just-in-time (JIT) compiled using `numba` to achieve $C-$like performance. Our branch simulator also uses multiple threads (24 threads on the two `2 six-core Intel Xeon X5670@2.93GHz` nodes) to explore multiple branches at the same time and it can explore a single branch in $\sim 18\,\mu s$. Because multithreading starts for $n_b > 10^3$ only, it is possible to see the small jump caused by the multithreading overhead. The inset of Fig. S15 shows the projected runtime on Summit by rescaling to Summit's $\texttt{R}_{\max}$ [70] ($\texttt{R}_{\max}^{\text{Summit}} = 200{,}794.9$ TFlops, $\texttt{R}_{\max}^{\text{Merope (single node)}} = 140.64$ GFlops), assuming that $|\psi_0\rangle$ and $|\psi_1\rangle$ can be fully stored in Summit (seed Fig. S16). In Fig. S16, we report the number of elements different from zero in $|\psi_0\rangle$ and $|\psi_1\rangle$. As one can see, the number of elements different from zeros scales as $2^{0.79\,N_D}$ and can be accommodated on single nodes (shaded area corresponds to the amount of virtual memory [RAM] used by the simulator). Because branches are explored using a depth-first search strategy, most of the virtual memory used by our branching algorithm is reserved to store $|\psi_0\rangle$ and $|\psi_1\rangle$, it would be in principle possible to simulate between $N_D \approx 50$ and $N_D \approx 60$ non-Clifford rotations on Summit before running out of virtual memory (Summit has 10 PB of available DDR4 RAM among its 4,608 nodes [71]).

C. Tensor Contraction

Tensor contraction is a powerful tool to simulate large quantum circuits [40, 58–62]. In our numerical simulations, we use tensor contraction to compute approximate OTOC values. It is well known that approximate amplitudes can be sampled by properly slicing the tensor network and only contracting a fraction of the sliced tensor networks [60, 61, 67, 68]. However, in our numerical simulations, we used a different approach to compute approximate OTOC values. More precisely, rather than computing one (approximate) amplitude at a time using tensor contraction, we compute (exact) "batches" of amplitudes by leaving some of the terminal qubits in the tensor network "open". Let
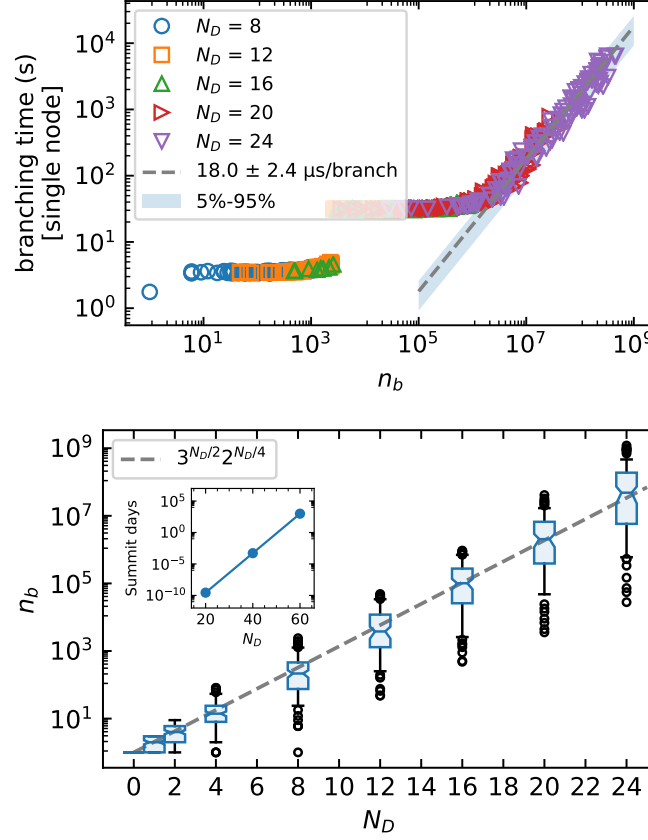
FIG. S15. (Top) Runtime (in seconds) to explore a given number of branches (results are for nodes with `2 six-core Intel Xeon X5670@2.93GHz`). (Bottom) Number n_b of explored branches by varying the number N_D of non-Clifford rotations (boxes extend from the lower to upper quartile values of the data, with a line at the median, while whiskers correspond to the $5\% - 95\%$ confidence interval). The inset shows the projected runtime on Summit.
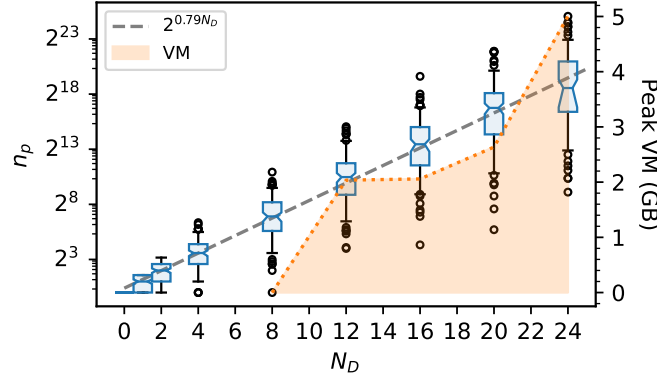

FIG. S16. Number n_p of bitstrings in $|\psi_0\rangle$ and $|\psi_1\rangle$ which are different from zero after applying the butterfly operator $\hat{C} = \hat{U}^\dagger \hat{\sigma}^{(Q_b)} \hat{U}$ to the initial state $|+\rangle$, by varying the number N_D of non-Clifford rotations. The shaded area correspond to the peak of the amount of virtual memory (RAM) used to simulate the OTOC circuits (95% among different simulations).

us call κ a given projection of the non-open qubits and us define $|\psi_0^{(\kappa)}\rangle$ and $|\psi_1^{(\kappa)}\rangle$ the projection of $|\psi_0\rangle = \sum_\kappa |\psi_0^{(\kappa)}\rangle$ and $|\psi_1\rangle = \sum_\kappa |\psi_1^{(\kappa)}\rangle$ respectively. Therefore, we can re-define the OTOC value as a "weighted" average of partial
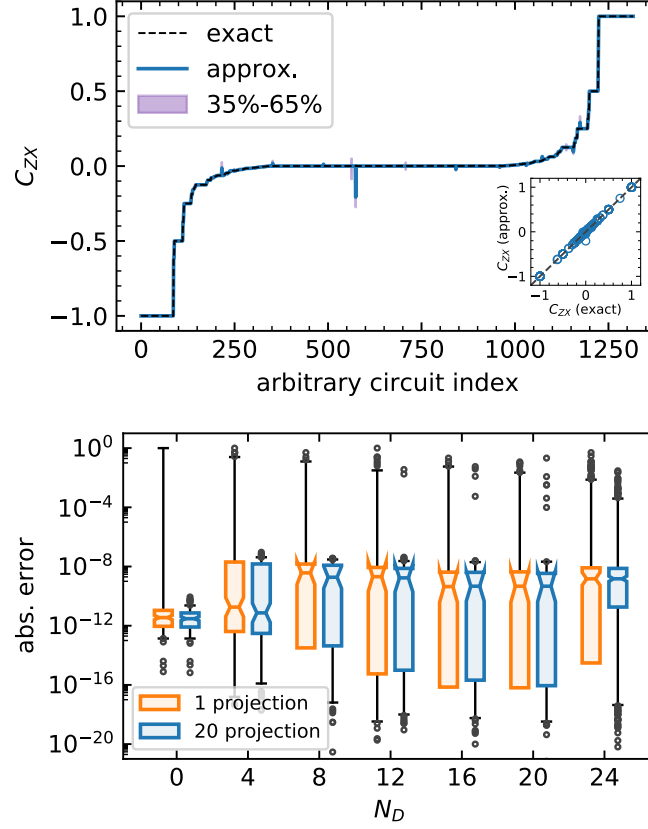
FIG. S17. (Top) Comparison between exact and approximate OTOC values (circuits are ordered accordingly to the exact OTOC value over different circuits with different depths, layouts and numbers of non-Clifford rotations). The Pearson coefficient between exact and approximate OTOC values is $R = 0.99987$. (Bottom) Absolute error by varying the number N_D of non-Clifford rotations (boxes extend from the lower to upper quartile values of the data, with a line at the median, while whiskers correspond to the $5\% - 95\%$ confidence interval).

OTOC values, that is:

$$\langle \hat{\sigma}_y \rangle := \frac{\sum_\kappa \omega_\kappa \langle \hat{\sigma}_y \rangle_\kappa}{\sum_\kappa \omega_\kappa}, \tag{S6}$$

with

$$\langle \hat{\sigma}_y \rangle_\kappa = \frac{\mathbb{R}\left[\langle \psi_1^{(\kappa)} | \psi_0^{(\kappa)} \rangle\right]}{\left(\|\psi_0^{(\kappa)}\|^2 + \|\psi_1^{(\kappa)}\|^2\right)/2} \tag{S7}$$

and $\omega_\kappa = \left(\|\psi_0^{(\kappa)}\|^2 + \|\psi_1^{(\kappa)}\|^2\right)/2$. It is interesting to observe that Eq. (S7) corresponds to the correlation coefficient between two non-normalized states and that the exact OTOC value is equivalent to the weighted average of single projection OTOC values. Indeed, when all κ are included, Eq. (S6) reduces to Eq. (S5). However, because $\langle \sigma_y \rangle$ needs to be $\mathcal{O}(1)$ to be experimentally measurable, few projection κ may actually be sufficient to get a good estimate of Eq. (S6).

In our numerical simulations, we left 24 qubits open and we used 20 random κ projections to compute an approximate OTOC value using Eq. (S6). If not indicated otherwise, medians and confidence intervals are computed by bootstrapping 1,000 times Eq. (S6) using 10 randomly chosen projections among the 20 available. Fig. S17 shows the comparison of approximate and exact OTOC values, by varying the circuit index (top) and by varying the number of non-Clifford rotations (bottom). As one can see, there is a great agreement between approximate and exact results across different circuits with different depth, layout and number of non-Clifford rotations (top). The bottom part of Fig. S17 shows the absolute error by varying the number of non-Clifford rotations. In particular, we are comparing results by averaging over single projections κ using Eq. (S7) (orange/light gray boxes) or by bootstrapping 1,000 times
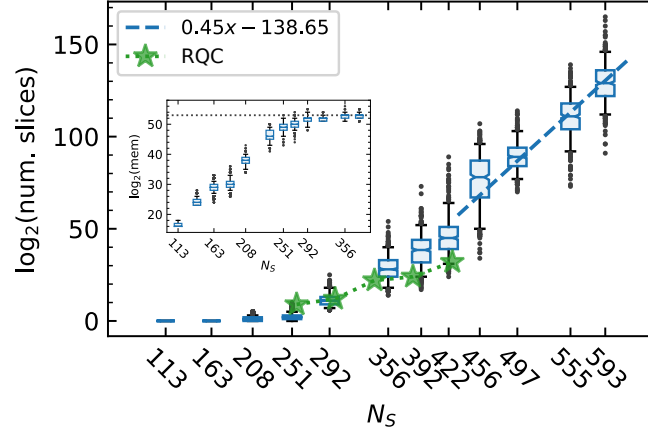
FIG. S18. Number of slices required to fit the largest tensor in memory during tensor contraction with a threshold of 2^{28} elements by varying the number N_S of iSWAPs (boxes extend from the lower to upper quartile values of the data, with a line at the median, while whiskers correspond to the $5\% - 95\%$ confidence interval). Green stars correspond to expected number of slices to compute single amplitudes of random quantum circuits (RQC) with a similar depth [38, 62]. (Inset) Number of elements to store in memory for the largest tensor during tensor contraction. For sufficiently deep circuits, the number of elements for the largest tensor saturates to the size of the Hilbert space 2^n, with $n = 53$ the number of qubits in the Sycamore chip.

Eq. (S6) using 10 randomly chosen projections among the 20 available (blue/dark gray boxes). As expected, results become less noisy by increasing the number of used projections.

Due to the limited amount of memory in HPC nodes, slicing techniques are required to fit the tensor contraction on a single node and avoid node-to-node memory communication overhead [61, 62]. In our numerical simulations, we used `cotengra` [62] and `quimb` [72] to identify the best contraction (including slicing) and perform the actual tensor contraction respectively. Because each different projection κ may lead to a slightly different simplification of the tensor network (in our numerical simulations, we used the rank and column reduction included in the `quimb` library), we recompute the best contraction for each single projection. For each projection (regardless of the depth/number of iSWAPs) we fixed `max_repeats = 128` in `cotengra` and restarted the heuristics 10 times to identify the optimal contraction (with a hard limit of 2 minutes for each run), using 24 threads on a `2 six-core Intel Xeon X5670@2.93GHz` node. We found that the runtime to the best contraction scales as $0.03 N_S - 3.68$ minutes, with N_S the number of iSWAPs in the circuit, that is less than 20 minutes for ~ 600 iSWAPs. Fig. S18 shows the number of slices required to have the largest tensor in the tensor contraction no larger than 2^{28} elements. Green stars in the figure correspond to the number of slices to compute single amplitudes of random quantum circuits with a similar number of iSWAPs [38, 62]. Because OTOC circuits and the random quantum circuits presented in [38] share a similar randomized structure, the computational complexity mainly depends on the number of iSWAPs (OTOC slicing is slightly worse because of the open qubits). We may expect an improvement in the slicing by using novel techniques as the "subtree reconfiguration" proposed by Huang *et al.* [40]. It is interesting to observe that, for deep enough circuits, the number of elements of the largest tensor in the tensor contraction saturates to the number of qubits (inset).

Fig. S19 summarizes the computational cost to compute an exact single projection κ. Top panel of Fig. S19 reports the actual runtime to contract a tensor network, by varying its expected total cost (including the slicing overhead) in FLOPs (expected FLOPs are using by `cotengra` to identify an optimal contraction). Dashed and dot-dashed lines correspond to the peak performance and expected performance of a `2 six-core Intel Xeon X5670@2.93GHz` node. The sustained performance of 64% is consistent with similar analysis on the NASA cluster [61]. Bottom panel reports the number of FLOPs (with and without the slicing overhead) by varying the number of iSWAPs. On the right y-axis, it is reported the extrapolated number of days to simulate OTOC circuits of a given number of iSWAPs, by assuming a sustained performance of 148,600 TFLOPs. Green stars corresponds to the total FLOPs (including the slicing overhead) to compute single amplitudes of random quantum circuits with a similar number of iSWAPs [62].

IV. MARKOV POPULATION DYNAMICS

For a broad class of circuit ensembles the average OTOC can be computed efficiently (in polynomial time) on a classical computer. This appears surprising as computing the output of the random circuit is expected to require
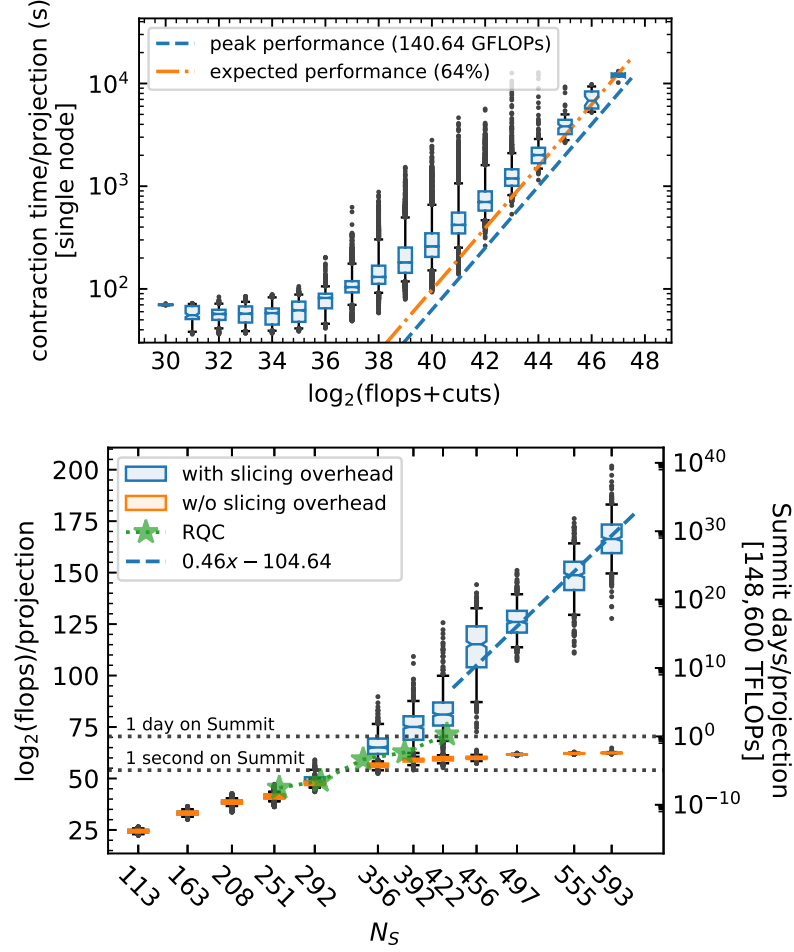
FIG. S19. (Top) Runtime (in seconds) to fully contract a single projection by varying the required number of FLOPs (results are for single nodes with `2 six-core Intel Xeon X5670@2.93GHz`). Because `long double` are used throughout the simulation, we used the conversion factor 8 to convert FLOPs to actual time. (Bottom) Flops to contract a single projection by varying the number N_S of iSWAPs, with and without the slicing overhead. Summit's days are obtained by using Summit's R_{peak} [70] and the conversion factor 8 from FLOPs to actual time (because `long double`'s have been used throughout the simulation). Green stars correspond to expected number of FLOPs to compute single amplitudes of random quantum circuits (RQC) with a similar number of iSWAPs [38, 62].

exponential resource. This contradiction is resolved by demonstrating an exact mapping of the average evolution of OTOC onto a Markov population dynamics process. Such connection was identified for Hamiltonian dynamics [11] and subsequently for simplified models of random circuits [18, 19] where uniformly random two-qubit gate was assumed. In practice, we implement a specific gate set consisting of "cycles" of the form $\prod_{\langle ij \rangle} \hat{G}_i \hat{G}_j \hat{U}_{ij}(\theta, \phi)$ applied to non-overlapping pairs of nearest neighbour qubits $\langle i, j \rangle$. For each pair a cycle consists of two single qubit gates $\hat{G}_i, \hat{G}_j$ and an entangling two-qubit gate,

$$\hat{U}_{i,j}(\theta, \phi) = e^{-\frac{i}{2}\theta(X_i X_j + Y_i Y_j) - \frac{i\phi}{2} Z_i Z_j}, \tag{S8}$$

parameterized by fixed angles θ, ϕ. The random instances are generated by drawing single qubit gates from a specific finite set $\left\{ \hat{G}_i \right\}$. We consider two sets corresponding to generators of single qubit Clifford group $\{\sqrt{X^{\pm 1}}, \sqrt{Y^{\pm 1}}\}$ and the set which in conjunction with any entangling two-qubit gate generates a universal set $\{\sqrt{X^{\pm 1}}, \sqrt{Y^{\pm 1}}, \sqrt{W^{\pm 1}}, \sqrt{V^{\pm 1}}\}$ introduced in Sec. I.

Average OTOC can be calculated by first considering the dynamics of the pair of butterfly operators $\hat{O}(t) = U^\dagger \hat{O} U$ evolved under circuit U. We introduce the average of the pair of the operators acting in the direct product of two

Hilbert spaces of the two replicas of the same circuit:

$$\hat{\mathcal{O}}^{(2)}(t) = \overline{\hat{O}(t) \otimes \hat{O}(t)} \equiv \overline{\hat{O}(t)^{\otimes 2}} \tag{S9}$$

where averaging over ensemble of the circuits is denoted by $\overline{(...)}$, and the rightmost equation defines the short-hand notation.

Analogously, one can introduce the higher order averages

$$\hat{\mathcal{O}}^{(4)}(t) = \overline{\hat{O}(t) \otimes \hat{O}(t) \otimes \hat{O}(t) \otimes \hat{O}(t)} \equiv \overline{\hat{O}(t)^{\otimes 4}}, \tag{S10}$$

as a starting point to analyze the circuit to circuit fluctuations of $C(t)$.

Then the value of OTOC is obtained by taking the matrix element of $C(t) = \langle \psi | \overline{\hat{M}\hat{O}(t)\hat{M}\hat{O}(t)} | \psi \rangle$ with the initial state that in our experimental setup is chosen to be $|\psi\rangle = \bigotimes_{i=1}^{n} |+\rangle_i$ where $|+\rangle_i$ is the symmetric superposition of the computational basis states. The average and the second moment of $C(t)$ are obtained as a straightforward convolution of the indices in Eqs. (S9) and (S10) respectively. Operator $\hat{\mathcal{O}}^{(4)}$ can be also used to study the effect of the initial state to the OTOC (clearly its average is not sensitive to the initial conditions).

A.   Symmetric single qubit gate set

We first consider average over uniformly random single qubits gate such that for any Pauli matrix,

$$\overline{\hat{\alpha}_i} \equiv \overline{\hat{G}^\dagger \hat{\alpha}_i \hat{G}} = 0, \tag{S11}$$

We will analyze the specific discrete gate sets used in the experiment in Section IV D. In this section, we use the Latin indices to label a qubit, and the Greek ones to denote the corresponding Pauli matrices $\hat{\alpha}_i = \{\hat{X}_i, \hat{Y}_i, \hat{Z}_i\}$

For a pair of operators as in Eq. (S9) there exist an analog of scalar product – a spherically symmetric combination that does not vanish after averaging,

$$\overline{\hat{\alpha}_i \otimes \hat{\beta}_j} = \overline{\hat{G}^\dagger \hat{\alpha}_i \hat{G} \otimes \hat{G}^\dagger \hat{\beta}_j \hat{G}} = \delta_{\alpha\beta}\delta_{ij}\mathcal{B}_i, \tag{S12}$$

where we introduced "bond" notation,

$$\mathcal{B}_i \equiv \frac{1}{3}\hat{\alpha}_i \otimes \hat{\alpha}_i \equiv \frac{1}{3}\left(\hat{X}_i^{\otimes 2} + Y_i^{\otimes 2} + Z_i^{\otimes 2}\right), \tag{S13}$$

and the summation over the repeated Greek indices is always implied.

Analogously one can find non-vanishing averages of the Pauli matrices acting in four replicas space of the same qubit (we will omit the qubit label). There are in total six bilinear combinations

$$\overline{\hat{\alpha} \otimes \hat{\beta} \otimes \hat{\mathbb{1}} \otimes \hat{\mathbb{1}}} = \delta_{\alpha\beta}\mathcal{B}^{(12)}, \quad \mathcal{B}^{(12)} = \frac{1}{3}\hat{\alpha} \otimes \hat{\alpha} \otimes \hat{\mathbb{1}} \otimes \hat{\mathbb{1}},$$

$$\overline{\hat{\alpha} \otimes \hat{\mathbb{1}} \otimes \hat{\beta} \otimes \hat{\mathbb{1}}} = \delta_{\alpha\beta}\mathcal{B}^{(13)}, \quad \mathcal{B}^{(12)} = \frac{1}{3}\hat{\alpha} \otimes \hat{\mathbb{1}} \otimes \hat{\alpha} \otimes \hat{\mathbb{1}}, \tag{S14a}$$

$$\vdots$$

$$\overline{\hat{\mathbb{1}} \otimes \hat{\mathbb{1}} \otimes \hat{\alpha} \otimes \hat{\beta}} = \delta_{\alpha\beta}\mathcal{B}^{(34)}, \quad \mathcal{B}^{(34)} = \frac{1}{3}\hat{\mathbb{1}} \otimes \hat{\mathbb{1}} \otimes \hat{\alpha} \otimes \hat{\alpha}.$$

Four cubic invariants are possible because there is no inversion operation for the spin:

$$\overline{\hat{\mathbb{1}} \otimes \hat{\alpha} \otimes \hat{\beta} \otimes \hat{\gamma}} = \epsilon^{\alpha\beta\gamma}\mathcal{C}^{(1)}, \quad \mathcal{C}^{(1)} \equiv \frac{\epsilon^{\alpha\beta\gamma}}{6}\hat{\mathbb{1}} \otimes \hat{\alpha} \otimes \hat{\beta} \otimes \hat{\gamma},$$

$$\overline{\hat{\alpha} \otimes \hat{\mathbb{1}} \otimes \hat{\beta} \otimes \hat{\gamma}} = \epsilon^{\alpha\beta\gamma}\mathcal{C}^{(2)}, \quad \mathcal{C}^{(2)} \equiv \frac{\epsilon^{\alpha\beta\gamma}}{6}\hat{\alpha} \otimes \hat{\mathbb{1}} \otimes \hat{\beta} \otimes \hat{\gamma}, \tag{S14b}$$

$$\vdots$$

$$\overline{\hat{\alpha} \otimes \hat{\beta} \otimes \hat{\gamma} \otimes \hat{\mathbb{1}}} = \epsilon^{\alpha\beta\gamma}\mathcal{C}^{(4)}, \quad \mathcal{C}^{(4)} \equiv \frac{\epsilon^{\alpha\beta\gamma}}{6}\hat{\alpha} \otimes \hat{\beta} \otimes \hat{\gamma} \otimes \hat{\mathbb{1}}.$$

where $\epsilon_{\alpha\beta\gamma}$ is the three-dimensional Levi-Civita symbol. Because they would change sign under the inversion operation, the cubic invariants can appear only in pairs on neighboring qubits.

Finally, the three quartic invariants are

$$\overline{\hat{\alpha} \otimes \hat{\beta} \otimes \hat{\gamma} \otimes \hat{\delta}} = \mathcal{D}^{(2)} \Upsilon_{\alpha\beta\gamma\delta} + \mathcal{D}^{(3)} \Upsilon_{\alpha\gamma\beta\delta} + \mathcal{D}^{(4)} \Upsilon_{\alpha\gamma\delta\beta},$$

$$\Upsilon_{\alpha\beta\gamma\delta} = \delta_{\alpha\beta}\delta_{\gamma\delta} - \frac{1}{4}\delta_{\alpha\gamma}\delta_{\beta\delta} - \frac{1}{4}\delta_{\alpha\delta}\delta_{\beta\gamma},$$

$$\mathcal{D}^{(2)} = \frac{2}{15}\hat{\alpha} \otimes \hat{\alpha} \otimes \hat{\beta} \otimes \hat{\beta}, \tag{S14c}$$

$$\mathcal{D}^{(3)} = \frac{2}{15}\hat{\alpha} \otimes \hat{\beta} \otimes \hat{\alpha} \otimes \hat{\beta},$$

$$\mathcal{D}^{(4)} = \frac{2}{15}\hat{\alpha} \otimes \hat{\beta} \otimes \hat{\beta} \otimes \hat{\alpha}.$$

This simple form implies the spherical symmetry of the single qubit averaging. For a lower symmetry (e.g. all the rotations of a cube) other quartic and cubic invariants are possible (like $X^{\otimes 4} + Y^{\otimes 4} + Z^{\otimes 4}$ or $|\epsilon_{\alpha\beta\gamma}|\hat{\mathbb{1}} \otimes \alpha \otimes \beta \otimes \gamma$) but we will ignore them for the sake of simplicity.

B. Efficient Population Dynamics for the Averaged OTOC

We expand average evolution of the pair of butterfly operators (S9) as,

$$\hat{O}^{(2)}(t) = \sum_{\{v_i\}} P_{\{v_i\}} \bigotimes_{i=1}^{n} \left(v_i \hat{\mathcal{B}}_i + u_i \hat{\mathbb{1}}_i^{\otimes 2} \right). \tag{S15}$$

where normalization condition reads,

$$u_i + v_i = 1, \tag{S16}$$

the variable $v_i = \{0, 1\}, i = 1, 2, ..., n$ indicates whether or not Pauli matrices occupy qubit i, and $P_{\{v_i\}}$ are formfactors. In other words, each ith is characterized either by $\rho_i^{(0)} \equiv \mathbb{1}_i^{\otimes 2}$, "vacuum", or the "bond" $\mathcal{B}_i$. All other terms in the right hand side of Eq. (S15) vanish upon averaging over single qubit gates see Sec. IV A.

Application of a two-qubit Sycamore gate to a pair of qubits $\{i, j\}$ is then described by $2^2 \times 2^2$ matrix in the space $\{v_i, v_j\}$,

$$\Omega = \begin{pmatrix} 1 & 0 & 0 & 0 \\ 0 & 1-a-b & a & b \\ 0 & a & 1-a-b & b \\ 0 & \frac{b}{3} & \frac{b}{3} & \left(1 - \frac{2}{3}b\right) \end{pmatrix}, \tag{S17}$$

$$a = \frac{1}{3}\left(2\sin^2\theta + \sin^4\theta\right),$$

$$b = \frac{1}{3}\left(\frac{1}{2}\sin^2 2\theta + 2\left(\sin^2\theta + \cos^2\theta\right)\right).$$

where the matrix Ω acts from the right on four dimensional row vector with the basis $(00), (01), (10), (11)$ The standard $\sqrt{\text{iSWAP}}$ gate corresponds to $\theta = \frac{\pi}{4}$, $a = \frac{1}{12}, b = \frac{1}{2}$, and iSWAP $\theta = \frac{\pi}{2}$ with $a = \frac{1}{3}, b = \frac{2}{3}$.

Each time when the two-qubit gate is applied the formfactor P is updated according to the rules

$$P_{v_1...v_i v_j...v_n}(t+1) = \sum_{v_i' v_j'} P_{v_1...v_i' v_j'...v_n}(t)\Omega_{v_i' v_j', v_i v_j}. \tag{S18}$$

Equations (S17)–(S18) are obtained by an application of a two-qubit gate (S8) with $\phi = 0$ to a pair (i, j) of factors in Eq. (S15) and averaging the result using Eqs. (S11) – (S12).

Some additional constraints can be extracted from the exact condition

$$\left[\hat{O}(t)\right]^2 = \bigotimes_{i=1}^{n} \hat{\mathbb{1}}_n. \tag{S19}$$

Convoluting operators in Eq. (S15), using $\hat{\mathbb{1}}_i^{\otimes 2} \to \hat{\mathbb{1}}_i$, $\hat{\mathcal{B}}_i \to \hat{\mathbb{1}}_i$ and the normalization condition (S16), we obtain the requirement

$$\sum_{\{v_i\}} P_{\{v_i\}}(t) = 1. \tag{S20}$$

Preserving this condition in the update rule (S18) requires the elements in each row of the matrix Ω from Eq. (S17) to add up to one. Moreover, all the elements of Ω are non-negative and therefore not only is $P_{\{v_i\}}(t)$ normalized but it is also non-negative.

Therefore, rules (S18) and (S20) defines the Markov process and variables $v_i = 0, 1$ correspond to the classical population of each qubit. As the non-populated states $v_i = v_j = 0$ do not evolve and the reproducing $(01) \to (11)$ and destruction $(11) \to (01)$ processes are allowed the problem (S18) is nothing but the classical population dynamics. The formfactors $P\left(v_1...v_i'v_j'...v_n, t\right)$ are interpreted as a distribution function over an n bit register $\{v_1...v_n\}$, subject to the Markov process defined by the update, Eq. (S17).

Direct solution of Eq. (S18) would require 2^n real numbers. However, unlike the original unitary evolution, the classical population dynamics involves only *positive* numbers constrained by normalization (S20). Such dynamics is very efficiently stimulated using a *classical* Monte Carlo type algorithm.

The butterfly operator is the starting point of the Markov process Eq. (S18). At long times the distribution $P_{\{v_i\}}$ converges to the stationary state $\bigotimes_{i=1}^n \rho_i^{(erg)}$, where $\rho_i^{(erg)} = \frac{1}{4}\left(\mathbb{1}_i^{\otimes 2} + 3\mathcal{B}_i\right)$, which corresponds to "vacuum" occurring on each site i with probability $p\left(\mathbb{1}_i^{\otimes 2}\right) = \frac{1}{4}$ and "bond" occurring with probability $p(\mathcal{B}_i) = 3/4$. OTOC in this limit takes the value corresponding to the random matrix statistics [73]. Intermediate dynamics of OTOC between these two limits is fully described by the Markov process Eq. (S18). It has a form of shock wave spreading from the initial butterfly operator to cover the whole system. Note that the choice of the two qubit gate parameter θ has a dramatic effect on the intermediate OTOC dynamics. As discussed in the main text $\theta = \pi/2$ corresponds to the probability of butterfly operator to spread equal one, and therefore spreading with maximum velocity equal to the light cone velocity and saturating the Lieb-Robinson bound. At any other value of θ probability to spread is less then one which results in diffusive broadening of the front, and the center of the front propagates with a butterfly velocity that is smaller than the light cone velocity.

C. Sign Problem in the Population Dynamics for OTOC Fluctuations

As we already mentioned, the analytic calculation of the OTOC for an individual circuit is impossible. One can expect, however, that it is possible to express the variance of the OTOC in terms of some products of classical propagators similarly to the analysis of the mesoscopic fluctuations in the disordered metals. The purpose of this subsection is to show that even such a modest task can not be efficiently undertaken.

The starting point is the expansion in terms of the single qubit rotations invariants (S14). Similarly to Eq. (S15), we write for $\hat{\mathcal{O}}^{(4)}$ of Eq. (S10)

$$\hat{\mathcal{O}}^{(4)}(t) = \sum_{\{\mathbf{V}_i\}} P_{\{\mathbf{V}_i\}} \bigotimes_{i=1}^n \mathbf{V}_i \cdot \hat{\mathcal{Q}}_i, \tag{S21}$$

where $\hat{\mathcal{Q}}_i$ is the vector with $14 = 1 + 6 + 4 + 3$ operator components given by invariants of Eq. (S10):

$$\begin{aligned}
\hat{\mathcal{Q}}_i &= \left[\hat{\mathbb{1}}_i^{\otimes 4}, \mathbf{b}, \mathbf{c}, \mathbf{d}\right]. \\
\mathbf{b} &= \left(\hat{\mathcal{B}}_i^{(12)}, ..., \hat{\mathcal{B}}_i^{(34)}\right), \\
\mathbf{c} &= \left(\hat{\mathcal{C}}_i^{(1)}, ..., \hat{\mathcal{C}}_i^{(4)}\right), \\
\mathbf{d} &= \left(\hat{\mathcal{D}}_i^{(2)}, \hat{\mathcal{D}}_i^{(3)}, \hat{\mathcal{D}}_i^{(4)}\right),
\end{aligned} \tag{S22}$$

and $\mathbf{V}_i$ are the 14 basis unit vectors so that 13 components equal to zero and the remaining component is 1. In other words, each site can be in 14 possible states.

A straightforward generalization of the evolution equation (S18) reads

$$P_{\mathbf{V}_1 \cdot \mathbf{v}_i \mathbf{v}_j \cdot \mathbf{v}_n}(t+1) = \sum_{\mathbf{V}_i' \mathbf{V}_j'} P_{\mathbf{V}_1 \cdot \mathbf{v}_i' \mathbf{v}_j' \cdot \mathbf{v}_n}(t) \boldsymbol{\Omega}_{\mathbf{V}_i' \mathbf{V}_j', \mathbf{V}_i \mathbf{V}_j}, \tag{S23}$$

where $\boldsymbol{\Omega}$ is now $14^2 \times 14^2$ whose explicit form is known but not quite important for the further consideration.

Equation (S23) involves 14^n real numbers. The only feasible path to the solution would be an efficient Monte Carlo sampling. Naively, one can hope to map the problem to the multicolored population dynamics. However, it is not possible as we explain below.

Reliable Monte Carlo sampling requires (1) normalizable and non-negative weights, and (2) absence of the correlations in contribution of different configurations. Let us demonstrate that both conditions do not hold for the evolution of formfactors in Eq. (S21). Once again, we use exact Eq. (S19). Convoluting third and fourth replica in $\hat{\mathcal{O}}^{(4)}(t)$ we obtain

$$\hat{\mathcal{O}}^{(4)}(t) \to \hat{\mathcal{O}}^{(2)}(t) \otimes \hat{\mathbb{1}}, \quad \hat{\mathbb{1}} \equiv \left[\bigotimes_{i=1}^{n} \hat{\mathbb{1}}_i \right]. \tag{S24}$$

Convolutions of the four operators (S14) yield

$$\mathcal{B}^{(12)} \to \mathcal{B}^{(3)} \equiv \frac{1}{3} \hat{\alpha} \otimes \hat{\alpha} \otimes \hat{\mathbb{1}},$$

$$\hat{\mathbb{1}}^{\otimes 4}, \mathcal{B}^{(34)} \to \hat{\mathbb{1}}^{\otimes 3},$$

$$\mathcal{B}^{(13)}, \ \mathcal{B}^{(14)} \to \mathcal{B}^{(2)} \equiv \frac{1}{3} \hat{\alpha} \otimes \hat{\mathbb{1}} \otimes \hat{\alpha},$$

$$\mathcal{B}^{(23)}, \ \mathcal{B}^{(24)} \to \mathcal{B}^{(1)} \equiv \frac{1}{3} \hat{\mathbb{1}} \otimes \hat{\alpha} \otimes \hat{\alpha},$$

$$\mathcal{C}^{(3)}, \mathcal{C}^{(4)} \to \mathcal{C} \equiv \frac{\epsilon^{\alpha\beta\gamma}}{6} \hat{\alpha} \otimes \hat{\beta} \otimes \hat{\gamma}, \tag{S25}$$

$$\mathcal{C}^{(1)} \to iB^{(1)}, \qquad \mathcal{C}^{(2)} \to iB^{(2)},$$

$$\mathcal{D}^{(2)} \to \frac{6}{5} \mathcal{B}^{(3)},$$

$$\mathcal{D}^{(3)} \to \frac{2}{5} \mathcal{B}^{(3)} + \frac{4i}{5} \mathcal{C},$$

$$\mathcal{D}^{(4)} \to \frac{2}{5} \mathcal{B}^{(3)} - \frac{4i}{5} \mathcal{C}.$$

Let us convolute both sides of Eq. (S21) using the rules (S24) – (S25). We find

$$\hat{\mathcal{O}}^{(2)}(t) \otimes \hat{\mathbb{1}} = \sum_{\{\mathbf{V}_i\}} P_{\{\mathbf{V}_i\}} \bigotimes_{i=1}^{n} \left(q_i^{(1)} + q_i^{(2)} + q_i^{(3)} + q_i^{(4)} \right),$$

$$q_i^{(1)} \equiv V_i^{(1)} \hat{\mathbb{1}}_i^{\otimes 3} + V_i^{(2)} \mathcal{B}_i^{(3)},$$

$$q_i^{(2)} \equiv V_i^{(7)} \hat{\mathbb{1}}_i^{\otimes 3} + \frac{2}{5} \left(3V_i^{(12)} + V_i^{(13)} + V_i^{(14)} \right) \mathcal{B}_i^{(3)},$$

$$q_i^{(3)} \equiv \left(V_i^{(3)} + V_i^{(4)} + iV_i^{(8)} \right) \mathcal{B}_i^{(1)}$$
$$+ \left(V_i^{(5)} + V_i^{(6)} + iV_i^{(9)} \right) \mathcal{B}_i^{(2)},$$

$$q_i^{(4)} \equiv \left(V_i^{(10)} + V_i^{(11)} + \frac{4i}{5} V_i^{(13)} - \frac{4i}{5} V_i^{(14)} \right) \mathcal{C}_i.$$

Here, the superscript in vector $V_i^{(\cdot)}$ enumerates components according to Eq. (S22). The total result is real as the imaginary terms are always generated in pairs.

Configurations with $V_i^{(1)} = u_i$, $V_i^{(2)} = v_i$, $V_i^{(3,..,14)} = 0$, exactly reproduce averaged result (S15). It means that all the other terms exactly cancel each other. It is possible only if the corresponding formfactors can be of both signs. Therefore, any finite unconstrained sampling leads to an arbitrary result (sign problem). Moreover, the constraints are non-local. Consider, e.g. cancellation of contribution proportional to $\mathcal{B}_i^{(1)} \mathcal{B}_j^{(1)}$. Cancellation occurs only if the formfactors different by replacement $V_i^{(8)} V_j^{(8)} \to V_i^{(a)} V_j^{(b)}$, $a, b = \{3, 4\}$ must be kept precisely the same. The requirement quickly becomes intractable with the increasing of the number of non-trivial matrices involved into cancellation.

To summarize, the general requirements on the evolution of the $\hat{\mathcal{O}}^{(4)}(t)$ lead to the sign and locality problems. Those two facts render a brute force classical Monte Carlo algorithm impossible. At present, we are not aware of any algorithm enabling to circumvent those obstacles.

D. Population Dynamics for iSWAP Gate Sets Implemented in the Main Text

Circuits with $\theta = \pi/2$ were used to realize Clifford as well as a universal ensemble. It is therefore instructive to study dynamics of the specific gate sets used in the experiment in more detail. Consider conjugation of a pair of Pauli operators $\hat{\alpha}_i \hat{\beta}_j$ by the iSWAP gate $\hat{S}$. It maps the pair onto another pair of Pauli operators $\hat{\gamma}_i \hat{\delta}_j$ according to the following rules,

$\hat{\alpha}_i \hat{\beta}_j$	$\hat{X}_i \hat{\mathbb{1}}_j$	$\hat{Y}_i \hat{\mathbb{1}}_j$	$\hat{Z}_i \hat{\mathbb{1}}_j$	$\hat{Z}_i \hat{X}_j$	$\hat{Z}_i \hat{Y}_j$	$\hat{\alpha}_i \hat{\alpha}_j$	$\hat{X}_i \hat{Y}_j$
$S^\dagger \hat{\alpha}_i \hat{\beta}_j S$	$-\hat{Z}_i \hat{Y}_j$	$\hat{Z}_i \hat{X}_j$	$\hat{\mathbb{1}}_i \hat{Z}_j$	$-\hat{Y}_i \hat{\mathbb{1}}_j$	$\hat{X}_i \hat{\mathbb{1}}_j$	$\hat{\alpha}_i \hat{\alpha}_j$	$\hat{Y}_i \hat{X}_j$

1. Clifford Gate Set

Clifford gate set used to obtain the data in the main text is drawn form the single qubit gate set $\{\hat{G}\} = \{\sqrt{X}, \sqrt{X^{-1}}, \sqrt{Y}, \sqrt{Y^{-1}}\}$. Averaging over this gates set of a symmetric pair of Pauli operators $\alpha_i \otimes \alpha_i$ reads,

$$\overline{\hat{G}^\dagger \hat{\alpha} \hat{G} \otimes \hat{G}^\dagger \hat{\alpha} \hat{G}} = \Xi_\alpha, \tag{S26}$$

where we introduce the basis $\Xi_\alpha = \{\mathbb{1}, \mathbb{X}, \mathbb{Y}, \mathbb{Z}\}$,

$$\mathbb{X} = \frac{1}{2}(\hat{Z}^{\otimes 2} + \hat{Y}^{\otimes 2}),$$

$$\mathbb{Y} = \frac{1}{2}(\hat{X}^{\otimes 2} + \hat{Z}^{\otimes 2}),$$

$$\mathbb{Z} = \frac{1}{2}(\hat{X}^{\otimes 2} + \hat{Y}^{\otimes 2}).$$

Single qubit gate average can be described in terms of the invariants $\Xi_\alpha \to M^{(S)}_{\alpha\beta} \Xi_\beta$,

$$M^{(S)} = \begin{pmatrix} 1 & 0 & 0 & 0 \\ 0 & 0 & \frac{1}{2} & \frac{1}{2} \\ 0 & \frac{1}{2} & 0 & \frac{1}{2} \\ 0 & \frac{1}{2} & \frac{1}{2} & 0 \end{pmatrix}. \tag{S27}$$

In this new basis $\{\Xi_\gamma \Xi_\delta\}$ instead of a 4×4 matrix Ω in Eq. (S17) effect of iSWAP gate is described by 16×16 matrix constructed straightforwardly from the rules Eqs. (S27) and the rules for iSWAP.

2. Universal Gate Set

The universal gates set used in the main text consists of eight choices of single qubit gates $\{\hat{G}\} = \{\sqrt{X^{\pm 1}}, \sqrt{Y^{\pm 1}}, \sqrt{W^{\pm 1}}, \sqrt{V^{\pm 1}}\}$. For the butterfly operator we choose $\hat{O}_i = \hat{X}_i$ the dynamics is described in the reduced subspace spanned by the basis $\Lambda = \{\mathbb{1}^{\otimes 2}, \hat{X}^{\otimes 2}, \hat{Y}^{\otimes 2}, \hat{Z}^{\otimes 2}\}$. Average of a pair of Pauli operators over this ensemble reads $\Lambda_\alpha \to M^{(U)}_{\alpha\beta} \Lambda_\beta$,

$$M^{(U)} = \begin{pmatrix} 1 & 0 & 0 & 0 \\ 0 & \frac{3}{8} & \frac{1}{4} & \frac{1}{2} \\ 0 & \frac{1}{8} & \frac{3}{8} & \frac{1}{2} \\ 0 & \frac{1}{2} & \frac{1}{2} & 0 \end{pmatrix}, \tag{S28}$$

Together with the rules for iSWAP gate it is straightforward to generate 16×16 matrix defining the Markov population dynamics process. Comparison of this noise-free population dynamics prediction for several different circuits with different locations of the butterfly operator X throughout the 53 qubit chip implemented experimentally is shown in Fig. S20.
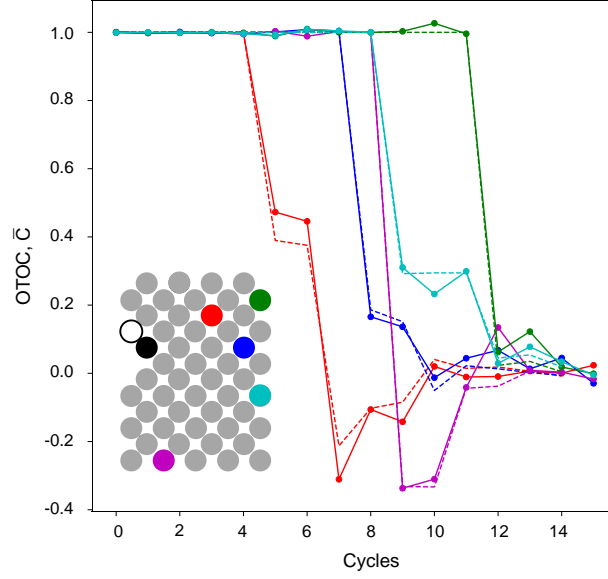
FIG. S20. Extended data for Fig. 2 in the main text: Average OTOC for four different locations of butterfly operator, X. Solid lines correspond to experimental data and dashed lines to the population dynamics simulation with Eq. (S28).

V. EFFICIENT POPULATION DYNAMICS FOR NOISY CIRCUITS

A. Inversion Error

The circuit to measure OTOC require inversion of gates $\hat{U}_{i,j}(\theta, \phi)$ which is not perfect. An important source of error is non-invertible phase ϕ such that instead of $\hat{U}_{i,j}^{\dagger}(\theta, \phi)$ the gate $\hat{U}_{i,j}(-\theta, \phi)$ is implemented. This inversion error can be included in the Markov population dynamics process in the following way,

$$
\Omega = \begin{pmatrix}
\cos^2 \phi & 0 & 0 & \sin^2 \phi \\
0 & 1 - \tilde{a} - b & \tilde{a} & b \\
0 & \tilde{a} & 1 - \tilde{a} - b & b \\
\frac{\sin^2 \phi}{9} & \frac{b}{3} & \frac{b}{3} & \frac{8 + \cos^2 \phi}{9} - \frac{2}{3} b
\end{pmatrix},
$$
$$
\tilde{a} = \frac{1}{3} \left(\cos^2 \phi \sin^4 \theta + \sin^2 \phi \cos^4 \theta \right).
$$

B. Generic Error Model

For an ensemble that satisfies Eq. (S11) the effect of relaxation and dephasing in the quantum processor can be captured by a one and two qubit depolarizing channel noise model,

$$
\rho \to (1 - p_1)\rho + \frac{p_1}{3} \sum_{\hat{\alpha} = \hat{X}, \hat{Y}, \hat{Z}} \hat{\alpha} \rho \hat{\alpha}, \tag{S29}
$$

$$
\rho \to (1 - p_2)\rho + \frac{p_2}{15} \sum_{\hat{\alpha}, \hat{\beta}} \hat{\alpha} \hat{\beta} \rho \hat{\alpha} \hat{\beta}. \tag{S30}
$$

In this case the Markov process Eq. (S17) can be modified in a straight forward way. For a single qubit depolarizing channel the Markov process Eq. (S17) is supplemented by the exponential decay rate as follows,

$$
\mathbb{1}_i^{\otimes 2} \to \mathbb{1}_i^{\otimes 2}, \tag{S31}
$$

$$
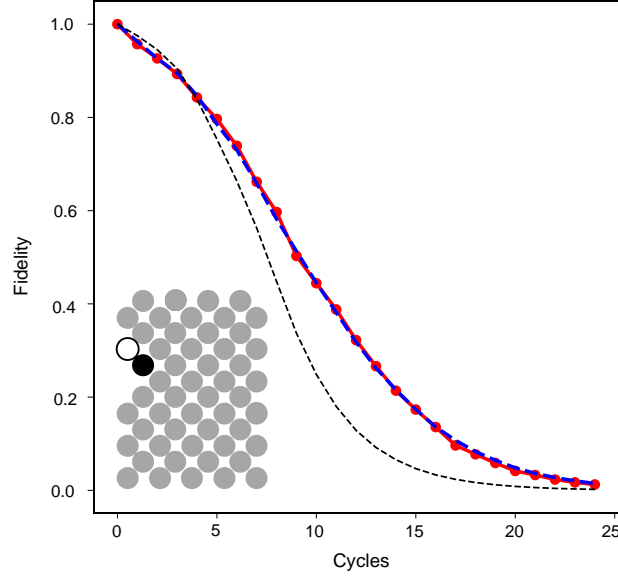\mathcal{B}_i \to e^{-4p_1/3} \mathcal{B}_i, \tag{S32}
$$

FIG. S21. Average fidelity of OTOC, i.e. the circuit with no butterfly applied shown as red line. OTOC fidelity from Monte Carlo simulation of noisy population dynamics Sec. V. The Pauli error rate $r_p = 0.013$ is determined by fitting the numerics to the experimental data. This value is within 10% of the gate fidelity determined in a separate experiment benchmarking two-qubit gates, see Sec. II. This is the single parameter of the model which is used to reproduce the rest of the OTOC data for 51 different locations of butterfly operator on the chip. Black dashed line shows a naive estimate of circuit fidelity via product of fidelities of gates within the light cone. Note that naive fidelity decays much faster with time than OTOC fidelity.

for each bond per gate cycle. Two-qubit depolarizing channel noise is accounted by supplementing the Markov process by the following,

$$\mathbb{1}_i^{\otimes 2}\mathbb{1}_j^{\otimes 2} \to \mathbb{1}_i^{\otimes 2}\mathbb{1}_j^{\otimes 2}, \tag{S33}$$

$$\mathcal{B}_i\mathbb{1}_j^{\otimes 2} \to e^{-\frac{16}{15}p_2}\mathcal{B}_i\mathbb{1}_j^{\otimes 2}, \tag{S34}$$

$$\mathcal{B}_i\mathcal{B}_j \to e^{-\frac{16}{15}p_2}\mathcal{B}_i\mathcal{B}_j. \tag{S35}$$

Note that the effect of noise on the Markov population dynamics cannot be described by the global depolarizing channel model that is often conjectured for ergodic circuits. Instead the time dependence of OTOC will demonstrate characteristic time dependence that can be used to verify the experimental data.

The described procedure allows us to verify the experimental results for average fidelity of OTOC circuits, the circuit with no butterfly applied, by direct comparison to the noisy population dynamics, see Fig. S21 and Fig. S22. We use the two-qubit Pauli error as a fitting parameter. Best fit corresponds to errors within 10% of the average error of two qubit cycle measured independently. We use the extracted error to predict values of OTOC for every position of the butterfly with no additional fitting. Comparison of the values of normalized OTOC predicted in this way with experimental data is shown in Fig. S23. This procedure introduces substantial noise-dependent bias into the observed OTOC values, which is illustrated in Fig. S24.

C. Error Mitigation for Average OTOC

We estimate circuit fidelity from the circuit shown in, Fig. 1 A, B, without the butterfly operator. This fidelity estimate is used for the error mitigation procedure aplied to the data in Fig. 2. In the error-free circuit absence of the butterfly operator means that U and $U^\dagger$ cancel each other exactly resulting in $C_{z0}(t) = 1$. In practice, inversion is imperfect as detailed in Sec. V A. Both errors in the unitary parameters and the effect of noise are reflected in the time dependence of $C_{z0}(t) < 1$ which serves as circuit fidelity, an analog of Loschmidt echo for local operator $\hat{M}$.
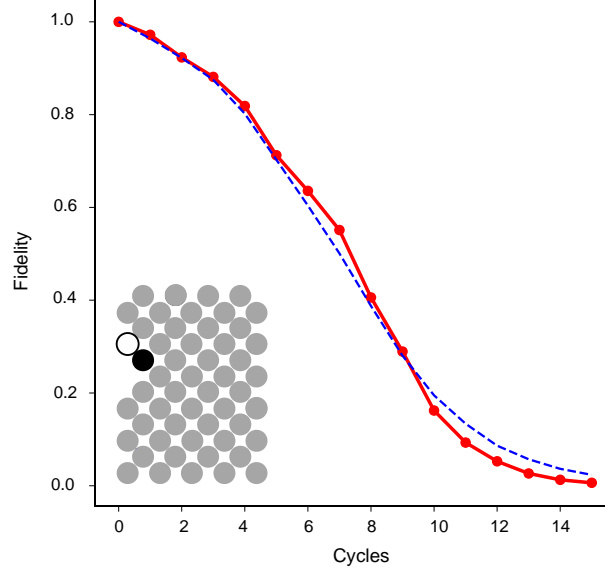
FIG. S22. OTOC circuits (with no butterfly applied) for universal iSWAP gate set. Solid red line shows experimental data and dashed blue line is the theoretical fit with a single parameter, Pauli error rate. The extracted Pauli error rate is $r_p = 0.012$ within 20% of the value obtained via two-qubit gate benchmarking.
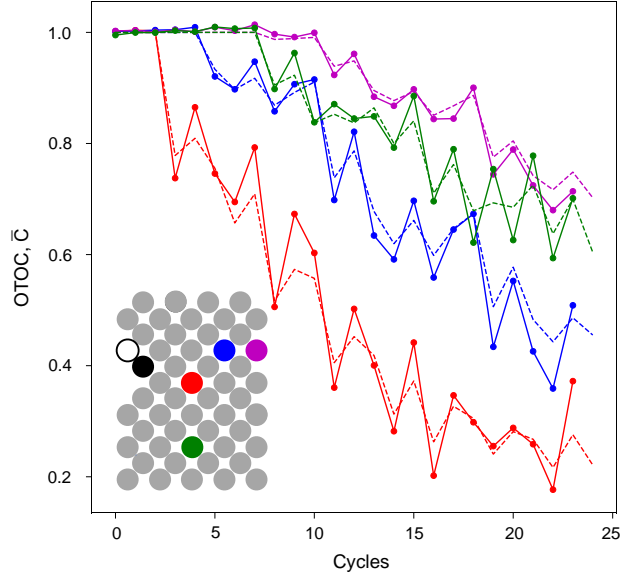

FIG. S23. Extended data for Fig. 2 of the main text: Normalized OTOC for four different locations of butterfly operator Z. Solid lines show experimental data, and dashed lines correspond to the noisy population dynamics.

Average over circuits reads,

$$\overline{C}_{0z} = \mathcal{F}_{\mathbb{1}_1^{\otimes 2}} + \mathcal{F}_{\mathcal{B}_1}, \tag{S36}$$

$$\overline{C}_{zz} = \mathcal{F}_{\mathbb{1}_1^{\otimes 2}} - \frac{1}{3}\mathcal{F}_{\mathcal{B}_1}. \tag{S37}$$

where the probabilities of vacuum $\mathcal{F}_{\mathbb{1}_1^{\otimes 2}}$ and bond $\mathcal{F}_{\mathcal{B}_1}$ at the measurement site are described by the population dynamics Eqs. (S17) with respective decay rates Eqs. (S31-S35). Note that the decay rate grows with the extent of spreading of the butterfly operator, resulting in the decay of fidelity that is not a simple exponent. Moreover,
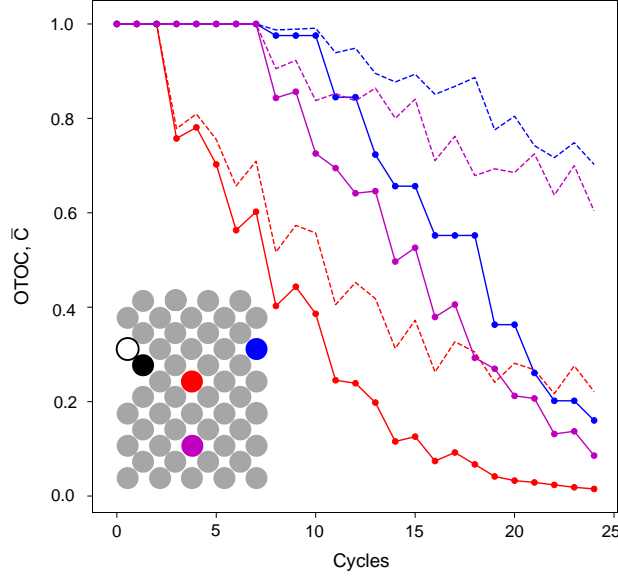
FIG. S24. Comparison of noisy OTOC obtained by normalization procedure, dashed lines, to noise-free population dynamics for the same circuit, solid lines.

in general $\mathcal{F}_{\mathbb{1}_1^{\otimes 2}}, \mathcal{F}_{\mathcal{B}_1}$ is not a simple probability no error occurred, as one could naively expect, see Fig. S21 for comparison.

The ratio of $\overline{C}_{zz}/\overline{C}_{0z}$ is compared to normalized data in Fig. S23. Note that this ratio does not correspond to the noise free OTOC, Fig. S24. This is because the probability of vacuum at measure site $\mathcal{F}_{\mathbb{1}_1^{\otimes 2}}$ decays slower with respect to its noise free value $p(\mathbb{1}_1^{\otimes 2})$ than the probability of the bond $\mathcal{F}_{\mathcal{B}_1}$. The latter corresponds to the weight of the operators which span the distance between measure and butterfly qubit which are more susceptible to noise. As a result normalized OTOC from noisy circuits overestimates the value of noise-free OTOC. For individual circuits such a simple description is no longer valid, as demonstrated by the dependence of fidelity estimate $C_{z0}(t)$ on the circuit instance, see Sec. VI. In many cases circuit dependent corrections are relatively small and the normalization procedure still works for individual circuits as well. Nonetheless, for our OTOC fluctuations data we develop a more efficient error mitigation procedure described in the following section.

D. Theory of Error Mitigation for Individual Circuits

We use a more precise error mitigation procedure for individual OTOC measurements presented in Figs. 3, 4 of the main text. These circuits contain iSWAP entangling gate and OTOC value can be expanded in terms of contributions from Clifford circuits. In presence of non-Clifford gates the butterfly operator can be conveniently expanded into Pauli strings B_i,

$$O(t) = \sum w_{\alpha_1 \ldots \alpha_n} B_{\alpha_1 \ldots \alpha_n},$$
$$B_{\alpha_1 \ldots \alpha_n} = \hat{\alpha}_1 \otimes \ldots \otimes \hat{\alpha}_n$$

For the initial state used in the experimental protocol $|\psi\rangle = \bigotimes |+\rangle_i$, the value of OTOC is expanded as,

$$C = \sum w_{\alpha \alpha_2 \ldots \alpha_n} w_{\beta \alpha_2 \ldots \alpha_n} \langle +_1 | \sigma_1^z \sigma_1^\alpha \sigma_1^z \sigma_1^\beta |+\rangle_1. \tag{S38}$$

The real part of the OTOC corresponds to $\alpha = \beta$,

$$\mathrm{Re}\, C = \sum w_{\alpha_1 \ldots \alpha_n}^2 \kappa_{\alpha_1}, \tag{S39}$$

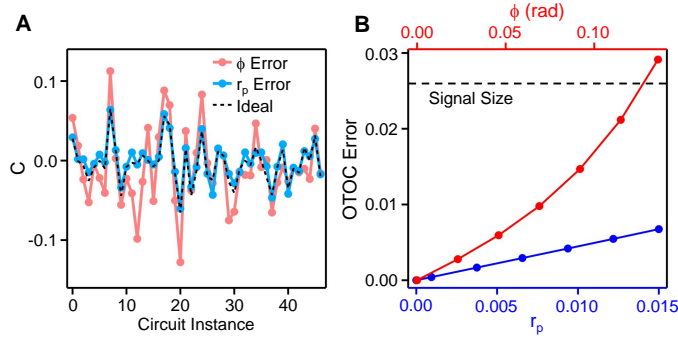where $\kappa_\alpha = \{1, -1, -1, 1\}$ for $\alpha = \{0, x, y, z\}$.

FIG. S25. Simulation of incoherent and coherent OTOC errors. (A) OTOCs, C, of 47 quantum circuit instances simulated in three different ways: with ϕ error, where a conditional-phase of 0.136 rad is added to every two-qubit gate; with r_{p} error, where a Pauli error of 0.015 is added to each two-qubit gate; ideal, where no error is introduced. The qubit configuration used here is a 1D chain of 10 qubits wherein Q_1 and Q_{b} reside at opposite ends of the chain. The two-qubit gate is iSWAP and $N_{\mathrm{D}} = 12$ non-Clifford gates are used for each instance. The number of circuit cycles is 34 ($N_{\mathrm{S}} = 250$). (B) The scaling of OTOC error (i.e. RMS deviation from the ideal OTOC values) against ϕ (red) and r_{p} (blue). Dashed line shows the size of the OTOC signal (i.e. RMS value of the ideal OTOCs).

For Clifford circuits ideal value of OTOC can be calculated efficiently. It can then be used to calculate circuit fidelity by comparing data with the expected value. The fidelity of the OTOC in presence of non-Clifford gates is then calculated by sampling a subset of OTOCs for Cliffords that appear in its expansion, see Eq. (S38). The fidelity is calculated by averaging over fidelities of individual Clifford contributions. Averaging reduces the circuit specific effect of noise and gives a more accurate estimate of fidelity.

VI.   NUMERICAL SIMULATION OF ERROR-LIMITING MECHANISMS FOR OTOC

In this section, we provide numerical simulation results aimed at identifying the potential error sources that limit our experimental accuracy in resolving OTOCs. As demonstrated in Section I, shot noise from finite statistical sampling is unlikely the dominant mechanism. The remaining known error channels are: 1. Incoherent, depolarizing noise in the quantum circuits, which can arise from qubit dephasing or relaxation. 2. Coherent errors in the quantum gates, e.g. the remnant conditional-phase ϕ demonstrated in Section II. We study each of these errors below.

A.   Coherent and Incoherent Contributions

We first describe how OTOC error from depolarizing noise may be simulated. We consider a depolarizing channel model parameterized by an error probability p,

$$\mathcal{E}(\rho) = (1 - p)\rho + p\frac{\mathbf{I}}{d}, \tag{S40}$$

where $d = 2^n$ is the dimension, and $\mathbf{I}$ the identity operator. The Kraus operators of this map are all Pauli strings of length n, where each non-trivial string has weight $\frac{p}{d^2}$. We consider a model where after each two qubit gate (these typically dominate the loss in fidelity compared to single-qubit gates), a two-qubit depolarizing channel is applied.

In Fig. S25A, we show a number of instance-dependent OTOC values C simulated using full density matrix calculations and an experimentally measured Pauli error rate r_{p} of 0.015 ($r_{\mathrm{p}} = 15p/16$ in Eq. (S40), due to the trivial Pauli string in the Kraus map from the identity matrix). Here we have used a smaller number of qubits due to the high cost of density-matrix simulation. To match with experiment, we have adjusted the number of circuit cycles to yield a total number of iSWAP gates close to those shown in Fig. 4 of the main text. The same normalization protocol as the experiment is also adopted, such that $\langle \hat{\sigma}_{\mathrm{y}} \rangle$ is simulated with and without the butterfly operator and their ratio is recorded as C. The results, compared to the ideal OTOC values also plotted in Fig. S25B, show little deviation.

Next, we simulate OTOCs of the same circuits with $r_{\mathrm{p}} = 0$ but an experimentally measured conditional-phase of $\phi = 0.136$ rad on each iSWAP gate and its inverse. The results are also plotted in Fig. S25A and seen to deviate much more from the ideal values. To quantify these observations, we have plotted the OTOC error as a function of
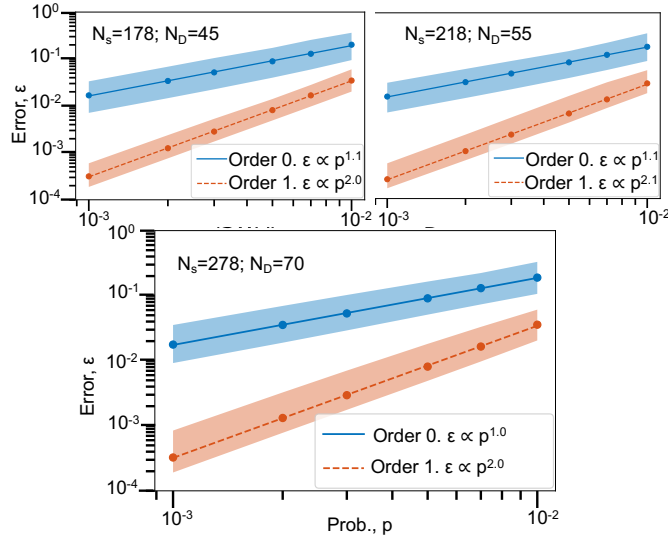
FIG. S26. Relative error ϵ of the 0'th and 1'st order error approximation (from Eq. (S41)) calculated by a pure state simulation, comparing to the exact value from a density matrix calculation, as a function of depolarizing probability p (Eq.(S40)). Here we compute C_{zx}, varying the number of iSWAP (N_s) and non-Clifford gates (N_D), with 11 qubits on a chain. The dots are the median over 48 circuits with lines of best fit given by the legend. The shaded region is the middle 50% of the data. The scaling of the error is close to $\epsilon \propto p^2$ as expected for the one-error approximation in all three cases.

both r_{p} and ϕ in Fig. S25B. Here we see that at the experimental limit ($r_{\mathrm{p}} = 0.015$ and $\phi = 0.136$ rad), the OTOC error is dominated by the contribution from ϕ (where it is ~ 0.03) rather than r_{p} (where it is ~ 0.006). Interestingly, the SNR is about 0.9 for $\phi = 0.136$ rad, which is close to the value measured in Fig. 4 of the main text for $N_{\mathrm{S}} \approx 250$.

Figure S25B also provides preliminary indication of how the OTOC accuracy for our experiments may be improved as we decrease both ϕ and r_{p}. We see that the OTOC error is linearly proportional to r_{p} whereas its scaling is steeper against ϕ. In particular, reducing ϕ by a factor of 2 leads to an OTOC error that is 3 times lower. Although these results may depend on the number of qubits and the structure of circuits, their similarity to experimental data nevertheless provides hints that reducing the conditional-phases in our iSWAP gates can potentially lead to large improvements in the OTOC accuracy. This can, for example, be achieved through concatenated pulses demonstrated in Ref. [51].

B. Perturbative Expansion of OTOC Error

The exact density-matrix calculation used in the preceding section is costly to implement and becomes quickly intractable as the number of qubits increase. One can more systematically estimate the instance specific noise contribution from a perturbation theory expansion of the quantum map Eq. (S40), with an entirely pure state calculation. Let us adopt the notation $\sigma_{m_1,m_2}^{(i,j)} = \sigma_{m_1}^{(i)}\sigma_{m_2}^{(j)}$, where $\sigma_m^{(i)}$ is the m'th Pauli operator ($m \in \{0, x, y, z\}$) applied on qubit i. We will also call $C[\sigma_{m_1,m_2}^{(i,j)}(d)]$ the OTOC value with the additional 'error gate' $\sigma_{m_1,m_2}^{(i,j)}$ inserted at layer d in the circuit. Then, to accuracy $O(p^2)$ one has

$$
\begin{aligned}
C_p = {} & (1-p)^{n_2} C_{\mathrm{ideal}} \\
& + \frac{p}{15}(1-p)^{n_2-1} \sum_{\substack{(m_1,m_2)\neq(0,0),\\ \langle i,j\rangle, d}} C[\sigma_{m_1,m_2}^{(i,j)}(d)],
\end{aligned}
\tag{S41}
$$

where C_{ideal} is the OTOC value in the limit of no noise, C_p the first order approximation of C_{ideal} in parameter p, and n_2 the total number of two-qubit gates in the circuit, occurring over pairs defined by $\langle i,j\rangle$ (i.e. Eq. (S41) is a sum over all error terms in the circuit). For convenience, we have also redefined $p \to 15p/16$ from Eq. (S40) due to the trivial contribution from the all zero Pauli string.

Eq. (S41) can be used to separate out the ideal OTOC value of an individual circuit, from the noise contribution. This noise contribution can be computed using $15 \times n_2$ circuit simulations (inserting each Pauli pair at all two-qubit gate locations in the circuit), though in some cases symmetries can be used to reduce this. For example, for the

normalization curve C_{z0}, only around half of this is required, since for each error in the reverse circuit $U^\dagger$, there is an equivalent one in U. Of course one can continue this expansion to arbitrary order, however the number of terms quickly becomes infeasible to compute (the k'th order contains $15 \times \binom{n_2}{k}$ terms).

In Fig. S26 we show the error scaling (comparing to an exact density matrix computation) for the zero'th (i.e. only the first term in Eq. (S41)) and first order approximation for C_{zx}, giving scaling in the error as expected; the error ϵ is computed as $|C_p(\text{exact}) - C_p(\text{approx})|/|C_p(\text{exact})|$, where $C_p(\text{approx})$ is from Eq. (S41), and $C_p(\text{exact})$ the value from the density matrix calculation with noise rate p. Moreover, the accuracy of the approximation remains fairly consistent, for a fixed noise level (p) for the three different circuit sizes (using a similar number of iSWAP gates as in the main text).

Here we have outlined a protocol of simulating the instance specific error contribution to the OTOC. This can be used to more accurately separate the instance specific OTOC value, systematic errors, and contributions from gate noise. Of course, the overhead in the simulation is a factor of $15n_2$, which can itself become challenging in deep enough circuits, although statistical sampling may be feasible in some cases.

VII.   OPERATOR ENTANGLEMENT AND OTOC VARIANCE

In this section we argue that OTOC variance is an observable witness of operator entanglement for the circuits with small number of non-Clifford gates considered in the main text. In the case of pure Clifford circuit OTOC variance equals unity indicating no operator entanglement. It decreases if non-Clifford gates are included in the circuit indicating generation of operator entanglement by the circuit. To justify this relationship further we provide an analysis of asymptotics and numerical simulations for practically implemented circuits. We demonstrate that there is a direct relationship between the long time asymptotics of the Schmidt measure, operator entanglement Renyi entropy and the variance of OTOCs for circuits with a sufficiently small number of non-Clifford gates. We finally demonstrate numerically that OTOC variance remains correlated with metrics of operator entanglement for the much shorter circuits implemented experimentally. Besides the circuits analyzed in this paper an alternative connection between operator entanglement and a generalization of OTOC was found under different circumstances in Ref. 74.

A.   Long time asymptotic of the OTOC variance

We consider a circuit acting on the operator $\hat{\mathcal{O}}$ consisting of $k + 1$ (multi-qubit) layers of gates,

$$\hat{\mathcal{O}}(t) = \hat{U}^\dagger(t)\hat{\mathcal{O}}\hat{U}(t), \tag{S42}$$

$$\hat{U}(t) = \hat{V}(t, t_k)\hat{V}(t_k, t_{k-1})...\hat{V}(t_1, 0), \tag{S43}$$

$$\hat{V}(t_{i+1}, t_i) \equiv \hat{U}_0(t_{i+1}, t_i)\hat{R}(t_i), \tag{S44}$$

consisting of Clifford segments $\hat{U}_0(t_{k+1}, t_k)$ (the product of all single and two-qubit gates applied between a pair of non-Cliffords) separated non-Clifford rotations $\hat{R}_i(t_{k+1})$.

We consider long time limit such that the Clifford segment $t_{k+1} - t_k$ is sufficiently long for ensemble average OTOCs to decay to their asymptotic values, equal to that of uniformly random unitaries (the so called Haar limit).

Consider expansion of $\hat{\mathcal{O}}(t_k)$ in the basis of n-qubit Pauli strings $\hat{\mathcal{P}}_\alpha$,

$$\hat{\mathcal{O}}(t_k) = \sum_\alpha \lambda_\alpha(t_k)\hat{\mathcal{P}}_\alpha, \tag{S45}$$

at the point in time t_k after the application of the last non-Clifford gate $\hat{R}(t_k)$, i.e. before application of $\hat{U}_0(t_{k+1}, t_k)$. Note that application of the Clifford segment will not change the number of terms in the expansion Eq. (S45). Moreover, the absolute value of coefficients wil remain the same. Application of the Clifford segment from t_k to $t_{k+1} = t$ conjugates the Pauli strings $\hat{\mathcal{P}}_\alpha(t) = \hat{U}_0^\dagger(t, t_k)\hat{\mathcal{P}}_\alpha\hat{U}_0(t, t_k)$ resulting in OTOC value,

$$C_{\mathcal{O}Z_1}(t_{k+1}) = \sum_{\alpha,\beta} \lambda_\alpha\lambda_\beta\Pi_{\alpha\beta}(t - t_k), \tag{S46}$$

where we introduced OTOCs of Pauli strings,

$$\Pi_{\alpha\beta}(t - t_k) \equiv \left\langle \hat{Z}_1\hat{\mathcal{P}}_\alpha(t - t_k)\hat{Z}_1\hat{\mathcal{P}}_\beta(t - t_k) \right\rangle. \tag{S47}$$
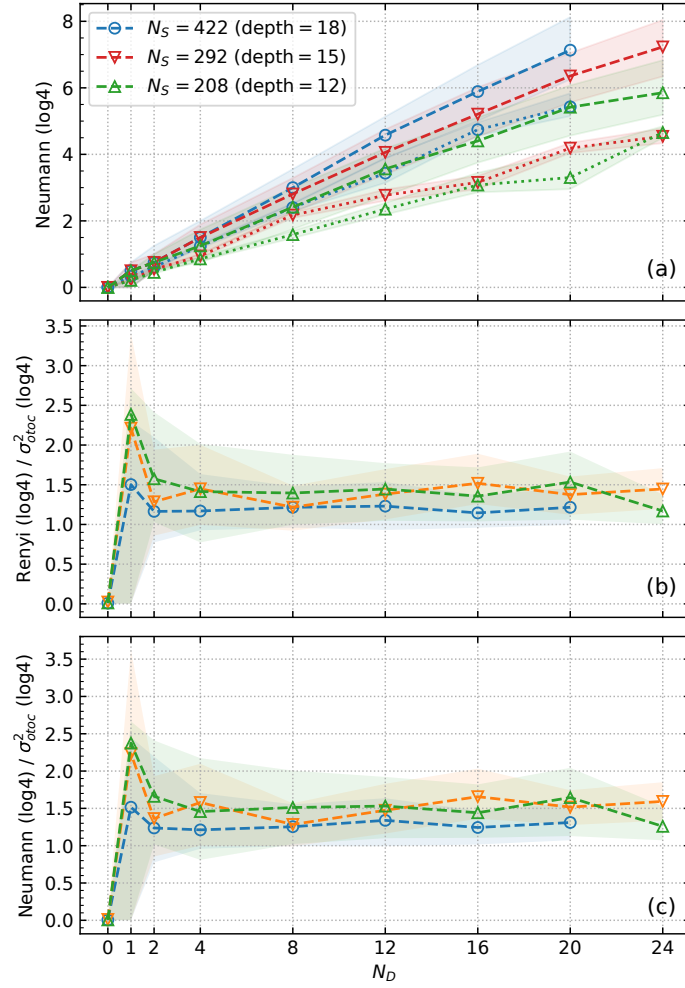
FIG. S27. Correlation between the OTOC fluctuations σ_{otoc}^2, the von Neumann entropy (Neumann $= -\sum_i \lambda_i^2 \log_4 \lambda_i^2$) and the Renyi entropy (Renyi $= -\log_4 \sum_i \lambda_i^4$), by varying the number of non-Clifford gates N_D for half Sycamore (25 qubits). (a) von Neumann entropy (dashed lines) compared to $-\log_4 \sigma_{otoc}^2$ (dotted lines). (b-c) Ratio between the von Neumann entropy (b) or Renyi entropy (c) to $-\log_4 \sigma_{otoc}^2$. As expected, both ratios are approaching to 1 by increasing the number of non-Clifford gates.

In terms of this expansion the square of OTOC reads,

$$C_{\mathcal{O}Z_1}^2 = \sum_{\alpha,\beta,\gamma,\delta} \lambda_\alpha \lambda_\beta \lambda_\gamma \lambda_\delta \Pi_{\alpha\beta}(t - t_k) \Pi_{\gamma\delta}(t - t_k). \tag{S48}$$

We introduce ensemble average $\overline{(\ldots)}$ over the last Clifford segment only. To calculate such ensemble averages of the Clifford segment we use the long time asymptotic, which corresponds to $\hat{\mathcal{P}}_\alpha(t), \hat{\mathcal{P}}_\beta(t)$ mapped onto random Pauli strings not equal to identity. Among such a set of $2^{2n} - 1$ Pauli strings $2^{2n}/2 - 1$ commute with $\hat{Z}_1$ and $2^{2n}/2$ do not. Therefore the ensemble average is given by the difference between the two,

$$\overline{\Pi_{\alpha\beta}} = -\frac{1}{2^{2n} - 1} \frac{\text{Tr}\{\hat{\mathcal{P}}_\alpha \hat{\mathcal{P}}_\beta\}}{2^n}. \tag{S49}$$

As discussed in the main text of the paper OTOC value for any specific Clifford circuit is $\Pi_{\alpha\alpha} = \pm 1$ and therefore average variance is simply,

$$\overline{\Pi_{\alpha\alpha}^2} = 1. \tag{S50}$$

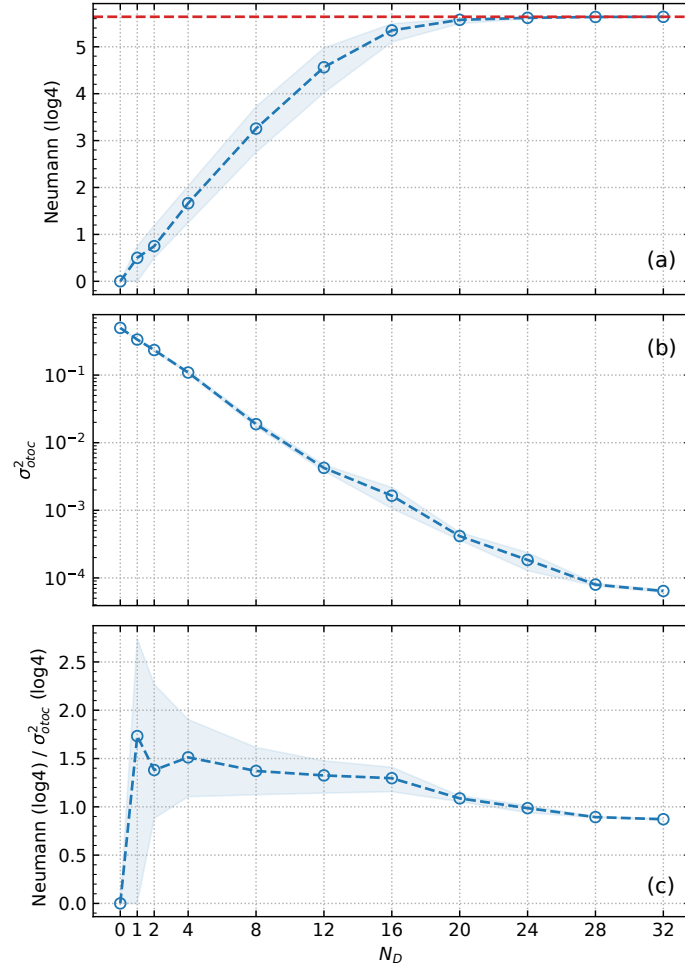In the same way we can estimate the cross-correlation terms. All average cross-correlations are either vanishing or

FIG. S28. Correlation between the OTOC fluctuations σ_{otoc}^2 and the von Neumann entropy (Neumann $= -\sum_i \lambda_i^2 \log_4 \lambda_i^2$), by varying the number of non-Clifford gates N_D for 6-qubit half chain. (a) von Neumann entropy. The red-dashed lines correspond to the expected saturation value of $(n \ln 2 - 1/2)/(2 \ln 2)$, with $n = 12$ being the size of the full chain. (b) The OTOC fluctuations defined as to $-\log_4 \sigma_{otoc}^2$. (c) Ratio between the von Neumann entropy to $-\log_4 \sigma_{otoc}^2$.

exponentially small $\alpha \neq \beta \neq \gamma \neq \delta$:

$$\overline{\Pi_{\alpha\beta}\Pi_{\beta\alpha}} = \frac{1}{2^n + 1}, \tag{S51a}$$

$$\overline{\Pi_{\alpha\beta}\Pi_{\alpha\beta}} = \frac{1}{2^n + 1}\frac{1}{2^n}\text{Tr}\{\hat{\mathcal{P}}_\alpha\hat{\mathcal{P}}_\beta\hat{\mathcal{P}}_\alpha\hat{\mathcal{P}}_\beta\}, \tag{S51b}$$

$$\overline{\Pi_{\alpha\alpha}\Pi_{\beta\beta}} = -\frac{1}{2^{2n} - 1}, \tag{S51c}$$

$$\overline{\Pi_{\alpha\alpha}\Pi_{\beta\gamma}} = 0, \tag{S51d}$$

$$\overline{\Pi_{\alpha\alpha}\Pi_{\alpha\beta}} = 0, \tag{S51e}$$

$$\overline{\Pi_{\alpha\beta}\Pi_{\gamma\delta}} \sim \frac{1}{2^{4n}}. \tag{S51f}$$

The effect of such cross-correlations on the sum in the expression for OTOC variance averaged over random Cliffords $\overline{C_{\mathcal{O}Z_1}^2}$, see Eq. (S48), are at most $\sim \lambda_\alpha^4 n_b^2/2^n \ll 1$. Neglecting terms of such order we obtain the average of Eq. (S48) in the form,

$$\overline{C_{\mathcal{O}Z_1}^2} \approx \sum_\alpha \lambda_\alpha^4. \tag{S52}$$
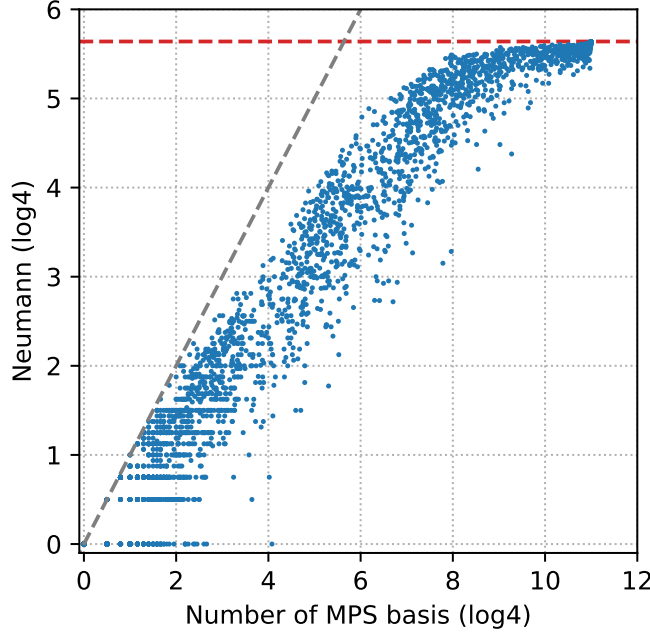
FIG. S29. Number of single-qubit MPS basis compared to the von Neumann entropy for a 6-qubit half chain. As one can see, there is a linear correlation between the two quantities up to the expected saturation value of $(n \ln 2 - 1/2)/(2 \ln 2)$, with $n = 12$ being the size of the full chain.

B. Metrics of operator entanglement

The simplest metric of operator entanglement for the time-evolved operator $\hat{\mathcal{O}}(t)$ is the Schmidt measure as introduced in the main text. Here we consider its connection to the more familiar metrics such as entanglement entropies.

Reduced density matrix of a half-system is introduced using the analogy between operators and states in a doubled space, see for example [75],

$$\rho_{ij} = \frac{1}{2^{2n}} \sum_k \text{Tr} \left\{ \hat{\mathcal{O}} \hat{a}_i \otimes \hat{b}_k \right\} \text{Tr} \left\{ \hat{\mathcal{O}} \hat{a}_j \otimes \hat{b}_k \right\}, \tag{S53}$$

where Pauli string bases in the two halves are,

$$\hat{a}_i \equiv \bigotimes_{s=1}^{n/2} \sigma_s^{i_s}, \quad \hat{b}_k \equiv \bigotimes_{s=\frac{n}{2}+1}^{n} \sigma_s^{k_s}, \tag{S54}$$

$k_s, i_s = 0, x, y, z$ and indexes i, j, k label respective Pauli strings.

Note that in presence of a small number of non-Cliffords, such that the number of terms in the expansion $\hat{\mathcal{O}}(t)$ is smaller than $2^{n/2}$ the reduced density matrix is dominated by its diagonal. Therefore, the Renyi operator entanglement entropy reads:

$$\overline{\text{Tr}\rho^2} \approx \sum_i \lambda_i^4, \tag{S55}$$

establishing a direct relationship between the asymptotics of OTOC variance and Renyi operator entanglement entropy.

C. Numerical Results

As described in the previous Section, the reduced density matrix ρ_{ij} is dominated by its diagonal. Therefore, it is possible to compute the exact eigenvalues of ρ_{ij}, including the numerical results for half-Sycamore ρ_{ij} with 25-

qubits, by identifying the small-sized blocks along the diagonal and compute the eigenvalues for each block. To identify these small sized blocks we use a simple cluster algorithm, with two indexes i and j being in the same cluster if $\rho_{ij} \neq 0$.

Fig. S27 correlates the OTOC fluctuations σ^2_{otoc}, the von Neumann entropy (Neumann $= -\sum_i \lambda_i^2 \log_4 \lambda_i^2$) and the Renyi entropy (Renyi $= -\log_4 \sum_i \lambda_i^4$), by varying the number of non-Clifford gates N_D. As expected, the ratio Neumann/σ^2_{otoc} (Fig. S27-b) and Renyi/σ^2_{otoc} (Fig. S27-c) approaches to 1 for a sufficiently large number of non-Clifford's. Similar results are shown in Fig. S28 for a 12-qubit chain.

Finally, Fig. S29 shows the correlation between the von Neumann entropy (half-chain) and the size of the single-qubit MPS basis set for a 12-qubit chain. The single-qubit MPS basis set is obtained by iteratively decomposing the operator $\hat{C}$ in Eq. S4 using a Schmidt decomposition. As expected, the size of the basis set is very well correlated to the von Neumann entropy up to its saturation value of $(n \ln 2 - 1/2)/(2 \ln 2)$, with $n = 12$ being the size of the full chain.

References and Notes

1. P. Hayden, J. Preskill, Black holes as mirrors: Quantum information in random subsystems. *J. High Energy Phys.* **2007**, 120 (2007). [doi:10.1088/1126-6708/2007/09/120](doi:10.1088/1126-6708/2007/09/120)

2. Y. Sekino, L. Susskind, Fast scramblers. *J. High Energy Phys.* **2008**, 65 (2008). [doi:10.1088/1126-6708/2008/10/065](doi:10.1088/1126-6708/2008/10/065)

3. N. Lashkari, D. Stanford, M. Hastings, T. Osborne, P. Hayden, Towards the fast scrambling conjecture. *J. High Energy Phys.* **2013**, 22 (2013). doi:10.1007/JHEP04(2013)022

4. W. Brown, O. Fawzi, Scrambling speed of random quantum circuits. arXiv:1210.6644 [quant-ph] (2013).

5. S. H. Shenker, D. Stanford, Black holes and the butterfly effect. *J. High Energy Phys.* **2014**, 67 (2014). doi:10.1007/JHEP03(2014)067

6. J. M. Deutsch, Quantum statistical mechanics in a closed system. *Phys. Rev. A* **43**, 2046–2049 (1991). doi:10.1103/PhysRevA.43.2046 Medline

7. M. Srednicki, Chaos and quantum thermalization. *Phys. Rev. E* **50**, 888–901 (1994). doi:10.1103/PhysRevE.50.888 Medline

8. M. Rigol, V. Dunjko, M. Olshanii, Thermalization and its mechanism for generic isolated quantum systems. *Nature* **452**, 854–858 (2008). doi:10.1038/nature06838 Medline

9. M. Blake, R. A. Davison, S. Sachdev, Thermal diffusivity and chaos in metals without quasiparticles. *Phys. Rev. D* **96**, 106008 (2017). doi:10.1103/PhysRevD.96.106008

10. D. Ben-Zion, J. McGreevy, Strange metal from local quantum chaos. *Phys. Rev. B* **97**, 155117 (2018). doi:10.1103/PhysRevB.97.155117

11. D. M. Basko, I. L. Aleiner, B. L. Altshuler, Metal–insulator transition in a weakly interacting many-electron system with localized single-particle states. *Ann. Phys.* **321**, 1126–1205 (2006). [doi:10.1016/j.aop.2005.11.014](doi:10.1016/j.aop.2005.11.014)

12. J. R. McClean, S. Boixo, V. N. Smelyanskiy, R. Babbush, H. Neven, Barren plateaus in quantum neural network training landscapes. *Nat. Commun.* **9**, 4812 (2018). [doi:10.1038/s41467-018-07090-4](doi:10.1038/s41467-018-07090-4) Medline

13. E. Knill, D. Leibfried, R. Reichle, J. Britton, R. B. Blakestad, J. D. Jost, C. Langer, R. Ozeri, S. Seidelin, D. J. Wineland, Randomized benchmarking of quantum gates. *Phys. Rev. A* **77**, 012307 (2008). doi:10.1103/PhysRevA.77.012307

14. J. Haferkamp, F. Montealegre-Mora, M. Heinrich, J. Eisert, D. Gross, I. Roth, Quantum homeopathy works: Efficient unitary designs with a system-size independent number of non-Clifford gates. arXiv:2002.09524 [quant-ph] (2020).

15. D. A. Roberts, D. Stanford, L. Susskind, Localized shocks. *J. High Energy Phys.* **2015**, 51 (2015). doi:10.1007/JHEP03(2015)051

16. I. L. Aleiner, L. Faoro, L. B. Ioffe, Microscopic model of quantum butterfly effect: Out-of-time-order correlators and traveling combustion waves. *Ann. Phys.* **375**, 378–406 (2016). [doi:10.1016/j.aop.2016.09.006](doi:10.1016/j.aop.2016.09.006)

17. D. A. Roberts, B. Yoshida, Chaos and complexity by design. *J. High Energy Phys.* **2017**, 121 (2017). doi:10.1007/JHEP04(2017)121

18. A. Nahum, S. Vijay, J. Haah, Operator Spreading in Random Unitary Circuits. *Phys. Rev. X* **8**, 021014 (2018). doi:10.1103/PhysRevX.8.021014

19. C. W. von Keyserlingk, T. Rakovszky, F. Pollmann, S. L. Sondhi, Operator Hydrodynamics, OTOCs, and Entanglement Growth in Systems without Conservation Laws. *Phys. Rev. X* **8**, 021013 (2018). doi:10.1103/PhysRevX.8.021013

20. T. Rakovszky, F. Pollmann, C. W. von Keyserlingk, Diffusive Hydrodynamics of Out-of-Time-Ordered Correlators with Charge Conservation. *Phys. Rev. X* **8**, 031058 (2018). doi:10.1103/PhysRevX.8.031058

21. P. Zanardi, Entanglement of quantum evolutions. *Phys. Rev. A* **63**, 040304 (2001). doi:10.1103/PhysRevA.63.040304

22. Although other classical pictures of operator spreading may arise for k-spin when k is close to infinity (*23*), they do not apply here since qubits are spin-1/2.

23. B. V. Fine, T. A. Elsayed, C. M. Kropf, A. S. de Wijn, Absence of exponential sensitivity to small perturbations in nonintegrable systems of spins 1/2. *Phys. Rev. E* **89**, 012923 (2014). doi:10.1103/PhysRevE.89.012923 Medline

24. J. Li, R. Fan, H. Wang, B. Ye, B. Zeng, H. Zhai, X. Peng, J. Du, Measuring Out-of-Time-Order Correlators on a Nuclear Magnetic Resonance Quantum Simulator. *Phys. Rev. X* **7**, 031011 (2017). doi:10.1103/PhysRevX.7.031011

25. M. Gärttner, J. G. Bohnet, A. Safavi-Naini, M. L. Wall, J. J. Bollinger, A. M. Rey, Measuring out-of-time-order correlations and multiple quantum spectra in a trapped-ion quantum magnet. *Nat. Phys.* **13**, 781–786 (2017). doi:10.1038/nphys4119

26. K. A. Landsman, C. Figgatt, T. Schuster, N. M. Linke, B. Yoshida, N. Y. Yao, C. Monroe, Verified quantum information scrambling. *Nature* **567**, 61–65 (2019). [doi:10.1038/s41586-019-0952-6](doi:10.1038/s41586-019-0952-6) Medline

27. M. S. Blok, V. V. Ramasesh, T. Schuster, K. O'Brien, J. M. Kreikebaum, D. Dahlen, A. Morvan, B. Yoshida, N. Y. Yao, I. Siddiqi, Quantum Information Scrambling on a Superconducting Qutrit Processor. *Phys. Rev. X* **11**, 021010 (2021). doi:10.1103/PhysRevX.11.021010

28. M. K. Joshi, A. Elben, B. Vermersch, T. Brydges, C. Maier, P. Zoller, R. Blatt, C. F. Roos, Quantum Information Scrambling in a Trapped-Ion Quantum Simulator with Tunable Range Interactions. *Phys. Rev. Lett.* **124**, 240505 (2020). doi:10.1103/PhysRevLett.124.240505 Medline

29. A. I. Larkin, Y. N. Ovchinnikov, Quasiclassical Method in the Theory of Superconductivity. *Sov. Phys. JETP* **28**, 1200 (1969).

30. B. Swingle, G. Bentsen, M. Schleier-Smith, P. Hayden, Measuring the scrambling of quantum information. *Phys. Rev. A* **94**, 040302 (2016). doi:10.1103/PhysRevA.94.040302

31. *C* in some cases can have a non-negligible imaginary part which is measured through the $\langle \hat{\sigma}_x \rangle$ of Q_a. For this work, we only measure the real part of *C* which is equal to $\langle \hat{\sigma}_y \rangle$ of Q_a.

32. B. Swingle, N. Yunger Halpern, Resilience of scrambling measurements. *Phys. Rev. A* **97**, 062113 (2018). doi:10.1103/PhysRevA.97.062113

33. B. Bertini, P. Kos, T. Prosen, Exact Correlation Functions for Dual-Unitary Lattice Models in 1+1 Dimensions. *Phys. Rev. Lett.* **123**, 210601 (2019). doi:10.1103/PhysRevLett.123.210601 Medline

34. P. W. Claeys, A. Lamacraft, Maximum velocity quantum circuits. *Phys. Rev. Res.* **2**, 033032 (2020). doi:10.1103/PhysRevResearch.2.033032

35. V. Khemani, D. A. Huse, A. Nahum, Velocity-dependent Lyapunov exponents in many-body quantum, semiclassical, and classical chaos. *Phys. Rev. B* **98**, 144304 (2018). doi:10.1103/PhysRevB.98.144304

36. Supplementary materials are available online.

37. D. Gottesman, The Heisenberg Representation of Quantum Computers. arXiv:quant-ph/9807006 [quant-ph] (1998).

38. F. Arute, K. Arya, R. Babbush, D. Bacon, J. C. Bardin, R. Barends, R. Biswas, S. Boixo, F. G. S. L. Brandao, D. A. Buell, B. Burkett, Y. Chen, Z. Chen, B. Chiaro, R. Collins, W. Courtney, A. Dunsworth, E. Farhi, B. Foxen, A. Fowler, C. Gidney, M. Giustina, R. Graff, K. Guerin, S. Habegger, M. P. Harrigan, M. J. Hartmann, A. Ho, M. Hoffmann, T. Huang, T. S. Humble, S. V. Isakov, E. Jeffrey, Z. Jiang, D. Kafri, K. Kechedzhi, J. Kelly, P. V. Klimov, S. Knysh, A. Korotkov, F. Kostritsa, D. Landhuis, M. Lindmark, E. Lucero, D. Lyakh, S. Mandrà, J. R. McClean, M. McEwen, A. Megrant, X. Mi, K. Michielsen, M. Mohseni, J. Mutus, O. Naaman, M. Neeley, C. Neill, M. Y. Niu, E. Ostby, A. Petukhov, J. C. Platt, C. Quintana, E. G. Rieffel, P. Roushan, N. C. Rubin, D. Sank, K. J. Satzinger, V. Smelyanskiy, K. J. Sung, M. D. Trevithick, A. Vainsencher, B. Villalonga, T. White, Z. J. Yao, P. Yeh, A. Zalcman, H. Neven, J. M. Martinis, Quantum supremacy using a programmable superconducting processor. *Nature* **574**, 505–510 (2019). [doi:10.1038/s41586-019-1666-5](doi:10.1038/s41586-019-1666-5) Medline

39. J. Gray, S. Kourtis, Hyper-optimized tensor network contraction. *Quantum* **5**, 410 (2021). [doi:10.22331/q-2021-03-15-410](doi:10.22331/q-2021-03-15-410)

40. C. Huang, F. Zhang, M. Newman, J. Cai, X. Gao, Z. Tian, J. Wu, H. Xu, H. Yu, B. Yuan, M. Szegedy, Y. Shi, J. Chen, Classical Simulation of Quantum Supremacy Circuits. arXiv:2005.06787 [quant-ph] (2020).

41. J. M. Kosterlitz, The critical properties of the two-dimensional xy model. *J. Phys. C Solid State Phys.* **7**, 1046–1060 (1974). [doi:10.1088/0022-3719/7/6/005](doi:10.1088/0022-3719/7/6/005)

42. D. S. Fisher, Critical behavior of random transverse-field Ising spin chains. *Phys. Rev. B* **51**, 6411–6461 (1995). doi:10.1103/PhysRevB.51.6411 Medline

43. Google AI Quantum and collaborators, Data and software code for "Information scrambling in quantum circuits", Zenodo (2021); https://doi.org/10.5281/zenodo.5548891.

44. P. Calabrese, F. H. L. Essler, G. Mussardo, Introduction to 'Quantum Integrability in Out of Equilibrium Systems'. *J. Stat. Mech.* **2016**, 064001 (2016). [doi:10.1088/1742-5468/2016/06/064001](doi:10.1088/1742-5468/2016/06/064001)

45. D. Gottesman, Class of quantum error-correcting codes saturating the quantum Hamming bound. *Phys. Rev. A* **54**, 1862–1868 (1996). doi:10.1103/PhysRevA.54.1862 Medline

46. B. M. Terhal, D. P. DiVincenzo, Classical simulation of noninteracting-fermion quantum circuits. *Phys. Rev. A* **65**, 032325 (2002). doi:10.1103/PhysRevA.65.032325

47. X. Wang, Entanglement in the quantum Heisenberg XY model. *Phys. Rev. A* **64**, 012313 (2001). doi:10.1103/PhysRevA.64.012313

48. V. Khemani, A. Lazarides, R. Moessner, S. L. Sondhi, Phase Structure of Driven Quantum Systems. *Phys. Rev. Lett.* **116**, 250401 (2016). doi:10.1103/PhysRevLett.116.250401 Medline

49. C. W. von Keyserlingk, S. L. Sondhi, Phase structure of one-dimensional interacting Floquet systems. II. Symmetry-broken phases. *Phys. Rev. B* **93**, 245146 (2016). doi:10.1103/PhysRevB.93.245146

50. R. K. Shukla, G. K. Naik, S. K. Mishra, Out-of-time-order correlation and detection of phase structure in Floquet transverse Ising spin system. arXiv:2002.05986 [cond-mat.stat-mech] (2020).

51. B. Foxen, C. Neill, A. Dunsworth, P. Roushan, B. Chiaro, A. Megrant, J. Kelly, Z. Chen, K. Satzinger, R. Barends, F. Arute, K. Arya, R. Babbush, D. Bacon, J. C. Bardin, S. Boixo, D. Buell, B. Burkett, Y. Chen, R. Collins, E. Farhi, A. Fowler, C. Gidney, M. Giustina, R. Graff, M. Harrigan, T. Huang, S. V. Isakov, E. Jeffrey, Z. Jiang, D. Kafri, K. Kechedzhi, P. Klimov, A. Korotkov, F. Kostritsa, D. Landhuis, E. Lucero, J. McClean, M. McEwen, X. Mi, M. Mohseni, J. Y. Mutus, O. Naaman, M. Neeley, M. Niu, A. Petukhov, C. Quintana, N. Rubin, D. Sank, V. Smelyanskiy, A. Vainsencher, T. C. White, Z. Yao, P. Yeh, A. Zalcman, H. Neven, J. M. Martinis; Google AI Quantum, Demonstrating a Continuous Set of Two-Qubit Gates for Near-Term Quantum Algorithms. *Phys. Rev. Lett.* **125**, 120504 (2020). doi:10.1103/PhysRevLett.125.120504 Medline

52. M. A. Nielsen, I. L. Chuang, *Quantum Computation and Quantum Information: 10th Anniversary Edition* (Cambridge Univ. Press, 2010).

53. D. C. McKay, C. J. Wood, S. Sheldon, J. M. Chow, J. M. Gambetta, Efficient Z gates for quantum computing. *Phys. Rev. A* **96**, 022330 (2017). doi:10.1103/PhysRevA.96.022330

54. S. Boixo, S. V. Isakov, V. N. Smelyanskiy, R. Babbush, N. Ding, Z. Jiang, M. J. Bremner, J. M. Martinis, H. Neven, Characterizing quantum supremacy in near-term devices. *Nat. Phys.* **14**, 595–600 (2018). [doi:10.1038/s41567-018-0124-x](doi:10.1038/s41567-018-0124-x)

55. G. Ithier, E. Collin, P. Joyez, P. J. Meeson, D. Vion, D. Esteve, F. Chiarello, A. Shnirman, Y. Makhlin, J. Schriefl, G. Schön, Decoherence in a superconducting quantum bit circuit. *Phys. Rev. B* **72**, 134519 (2005). doi:10.1103/PhysRevB.72.134519

56. E. Jeffrey, D. Sank, J. Y. Mutus, T. C. White, J. Kelly, R. Barends, Y. Chen, Z. Chen, B. Chiaro, A. Dunsworth, A. Megrant, P. J. J. O'Malley, C. Neill, P. Roushan, A.

Vainsencher, J. Wenner, A. N. Cleland, J. M. Martinis, Fast accurate state measurement with superconducting qubits. *Phys. Rev. Lett.* **112**, 190504 (2014). doi:10.1103/PhysRevLett.112.190504 Medline

57. M. B. Hastings, Observations outside the light cone: Algorithms for nonequilibrium and thermal states. *Phys. Rev. B* **77**, 144302 (2008). doi:10.1103/PhysRevB.77.144302

58. I. L. Markov, Y. Shi, Simulating Quantum Computation by Contracting Tensor Networks. *SIAM J. Comput.* **38**, 963–981 (2008). doi:10.1137/050644756

59. J. Chen, F. Zhang, C. Huang, M. Newman, Y. Shi, Classical Simulation of Intermediate-Size Quantum Circuits. arXiv:1805.01450 [quant-ph] (2018).

60. B. Villalonga, D. Lyakh, S. Boixo, H. Neven, T. S. Humble, R. Biswas, E. G. Rieffel, A. Ho, S. Mandrà, Establishing the quantum supremacy frontier with a 281 Pflop/s simulation. *Quantum Sci. Technol.* **5**, 034003 (2020). doi:10.1088/2058-9565/ab7eeb

61. B. Villalonga, S. Boixo, B. Nelson, C. Henze, E. Rieffel, R. Biswas, S. Mandrà. A flexible high-performance simulator for verifying and benchmarking quantum circuits implemented on real hardware. *npj Quantum Inf.* **5**, 86 (2019). doi:10.1038/s41534-019-0196-1

62. J. Gray, S. Kourtis, Hyper-optimized tensor network contraction. arXiv:2002.01935 [quant-ph] (2021).

63. S. Aaronson, D. Gottesman, Improved simulation of stabilizer circuits. *Phys. Rev. A* **70**, 052328 (2004). doi:10.1103/PhysRevA.70.052328

64. S. Bravyi, D. Gosset, Improved Classical Simulation of Quantum Circuits Dominated by Clifford Gates. *Phys. Rev. Lett.* **116**, 250501 (2016). doi:10.1103/PhysRevLett.116.250501 Medline

65. S. Bravyi, D. Browne, P. Calpin, E. Campbell, D. Gosset, M. Howard, Simulation of quantum circuits by low-rank stabilizer decompositions. *Quantum* **3**, 181 (2019). doi:10.22331/q-2019-09-02-181

66. S. Boixo, S. V. Isakov, V. N. Smelyanskiy, H. Neven, Simulation of low-depth quantum circuits as complex undirected graphical models. arXiv:1712.05384 [quant-ph] (2017).

67. I. L. Markov, A. Fatima, S. V. Isakov, S. Boixo, Quantum Supremacy Is Both Closer and Farther than It Appears. arXiv:1807.10749 [quant-ph] (2018).

68. I. Markov, A. Fatima, S. Isakov, S. Boixo, Faster classical sampling from distributions defined by quantum circuits. *APS Meet. Abstr.* **2019**, K42 (2019).

69. NASA Ames Research Center, "Merope Supercomputer" (2021); https://nas.nasa.gov/hecc/resources/merope.html.

70. M. Meuer, H. Simon, J. Dongarra, E. Strohmaier, H. W. Meuer, "November 2020" (Top500 List, 2020); www.top500.org/lists/top500/2020/11/.

71. Oak Ridge National Laboratory (ORNL), "Summit" (US Department of Energy, 2021); www.olcf.ornl.gov/olcf-resources/compute-systems/summit/.

72. J. Gray, quimb: A python package for quantum information and many-body calculations. *J. Open Source Softw.* **3**, 819 (2018). doi:10.21105/joss.00819

73. B. Yoshida, A. Kitaev, Efficient decoding for the Hayden-Preskill protocol. arXiv:1710.03363 [hep-th] (2017).

74. G. Styliaris, N. Anand, P. Zanardi, Information Scrambling over Bipartitions: Equilibration, Entropy Production, and Typicality. *Phys. Rev. Lett.* **126**, 030601 (2021). doi:10.1103/PhysRevLett.126.030601 Medline

75. T. Zhou, D. J. Luitz, Operator entanglement entropy of the time evolution operator in chaotic systems. *Phys. Rev. B* **95**, 094206 (2017). doi:10.1103/PhysRevB.95.094206